Tracing The Source and Transport of Atmospheric Water Vapor Using Stable Isotope Techniques

A MASTERS THESIS

SUBMITTED TO THE FACULTY OF THE GRADUATE SCHOOL

OF THE UNIVERSITY OF MINNESOTA

BY

Natalie M. Schultz

IN PARTIAL FULFILLMENT OF THE REQUIREMENTS

FOR THE DEGREE OF MASTER OF SCIENCE

Timothy J. Griffis, Advisor

December 2011

Acknowledgements

I would first like to thank my advisor, Tim Griffis, and my committee members, John Baker and John Nieber. I would not have been able to complete this work without their guidance and support. I would also like to thank the members of the Biometeorology Group, Ming Chen, Matt Erickson, Jeremy Smith, Joel Fassbinder, and Peter Turner for all of their moral support and technical assistance. I would especially like to thank Matt Erickson for his invaluable help with field and laboratory work, and Jeremy Smith for teaching me how to use Matlab. I would also like to thank Bill Brieter at the USDA-ARS for his assistance in the field. Financial support for this project was provided by the U.S. Department of Energy (DE-FG02-06ER64316), the National Science Foundation (ATM-0546476, ATM-0914473, DEB-0514908), and the College of Food, Agriculture, and Natural Resource Sciences at the University of Minnesota. Lastly, I would like to thank Doug Rudolph and my family and friends for supporting me throughout these last two years.

Abstract

The stable isotopes of hydrogen and oxygen in water can be used as environmental tracers of the hydrological and climate systems. The isotope ratios ($^{18}O/^{16}O$, $^{2}H/^{1}H$) of water are uniquely altered by biological and physical environmental processes, making them useful tracers of the origin and transport of water throughout the atmosphere and biosphere. Technological advancements have been made that allow continuous measurements of $\delta^{18}O$ and $\delta^{2}H$ in the vapor phase, and have simplified the isotope analysis of liquid water. The objectives of this thesis were two-fold: (1) to address a methodological problem that has prevented the use of isotope ratio infrared spectroscopy (IRIS) analyzers in the isotope analysis of water extracted from plant and soil samples, and (2) utilize tall tower measurements of $\delta^{18}O$ and $\delta^{2}H$ to develop a landscape-scale understanding of the mechanisms that control isotope variations in water vapor over a range of temporal scales. The correction procedure developed for the isotope analysis of plant and soil waters using an IRIS analyzer was found to greatly reduce the erroneous isotope values, resulting in a viable alternative to the traditional method of isotope ratio mass spectrometry (IRMS) for the isotope analysis of plant and soil waters. The observed temporal variations in $\delta^{18}O$, $\delta^{2}H$, and d in water vapor resulted from a combination of local and distant biophysical processes, including boundary layer dynamics, seasonal changes in evapotranspiration (ET), and Rayleigh rainout processes. The use of these new measurements of $\delta^{18}O$ and $\delta^{2}H$ in the vapor phase, along with models and satellite observations will provide new information on the transport and recycling of water vapor in the atmosphere, and ultimately help diagnose changes in the atmospheric water cycle in response to climate change and land use change.

Contents

List of Tables

List of Figures

Chapter 1

Thesis Introduction

The stable isotopes of hydrogen and oxygen in water have long been used to document and diagnose variations in the hydrological cycle and climate. For instance, the isotope ratios ($^{18}O/^{16}O$, $^{2}H/^{1}H$) of water have been used as proxies to reconstruct historical changes in temperature, humidity, and precipitation (Steffensen et al., 2008; Wright and Leavitt, 2006; Petit et al., 1999). Because the isotope ratios of $^{18}O/^{16}O$ and $^{2}H/^{1}H$ are predictably altered by biological and physical environmental processes, they can be used as forensic tracers of the water cycle and indicators of environmental change.

Human activities are altering earth's climate at a pace unprecedented in the past 650,000 years. Global concentrations of carbon dioxide (CO_2), methane (CH_4), and nitrous oxide (N_2O) have increased dramatically since 1750, with current levels of all three gases far exceeding any natural levels determined from historical ice core data. Global temperatures have steadily increased over time with higher concentrations of greenhouse gases. Global temperatures have increased 0.36^{o}F per decade since the late 1970s, with

2010 and 2005 tied as the warmest years on record since 1880 (Hansen et al., 2010). These trends in global temperature are expected to continue due to ongoing anthropogenic emissions of greenhouse gases. Although increases in surface temperatures are an easily measured indicator of climate change, changes in the atmospheric water cycle (i.e. humidity, evaporation, precipitation patterns) are additional consequences of human activities.

Climate change initiated by anthropogenic emissions of greenhouse gases has two important impacts on the hydrological cycle: (1) intensification of the cycle itself, and (2) a positive feedback on surface warming caused by increases in atmospheric water vapor. The intensification of the hydrologic cycle, an increase in evaporation, evapotranspiration (ET), and precipitation rates (Huntington, 2010), is expected to be one of the most important consequences of climate change (IPCC, 2007; Held and Soden, 2000). Theoretically, evaporation rates are expected to increase with surface temperature trends, along with the moisture-holding capacity of the air. The Clausius-Clapeyron equation predicts water vapor increases of about 7% per 1^{o}C at typical lower-troposphere temperatures (Held and Soden, 2000). Water vapor is the dominant greenhouse in earth's atmosphere, accounting for 60% of the greenhouse effect (Keihl and Trenberth, 1997). Because water vapor is expected to increase with surface temperature increases, and because water vapor is a powerful greenhouse gas, changes in the concentrations of atmospheric water vapor may amplify the initial warming caused by anthropogenic greenhouse gases.

Positive trends in atmospheric water vapor have been observed globally and over the central United States (McCarthy et al., 2009; Trenberth et al., 2005; Dai, 2006). Increas-

ing atmospheric water vapor is the primary cause of a more intense precipitation regime at mid to high latitudes in model simulations Dai (2006). Modeling experiments show that the widespread variability in precipitation is directly linked to variations in evaporation (Hall and Manabe, 2000). There has been a widespread increase in the frequency of very heavy precipitation over the last 50-100 years in the mid-latitudes (Groisman et al., 2005). Positive precipitation trends are observed locally, with the Minnesota state-averaged precipitation reaching a maximum level of 35 inches in 2010, a 26% increase since the first recorded measurements in 1890 (www.climate.umn.edu).

Quantifying the trends in evaporation or ET is more difficult because of the absence of long-term direct measurements. Indirect measurements of ET using the water-balance method indicate that ET has increased in the Mississippi River Basin at a rate of 0.95 to 1.04 mm year^{-1} since about 1950 (Qian et al., 2007; Walter et al., 2004; Milly and Dunne, 2001). Law et al. (2002) found that direct measurements of ET using the eddy-covariance method are positively correlated with growing-season temperature (19.7 mm ET per ^{o}C) for humid regions in the Fluxnet network (http://daac.ornl.gov/FLUXNET/fluxnet.shtml). For regions that are not water-limited, ET may theoretically increase with rising temperatures. Recently, Jung et al. (2010) found negative trends in global ET after 1997, likely due to soil-moisture limitations. If the limit of hydrological cycle intensification caused by surface warming has been reached, the likely future implications may include decreased terrestrial productivity and carbon sink, and accelerated surface warming.

At a regional scale, understanding the processes that control the trends in water vapor is more complex, depending on a number of regional factors such as atmospheric circula-

tion patterns, land use change, changes in water use patterns, agriculture intensification, and others. Although the trends in the atmospheric water cycle in this region have been well documented, the biological and physical mechanisms controlling these trends are considerably less known. The impacts of increased atmospheric water vapor and a more intense hydrological cycle are likely to be significant, but are highly uncertain because of the complex role of water vapor in the climate system, and the spatial variability of water vapor trends due to different feedbacks and forcing factors. A better understanding of the processes that control the transport of atmospheric moisture are important in order to (1) anticipate future changes in the atmospheric water cycle and subsequent ecosystem responses, and to (2) prepare societal adaptation strategies.

The isotopic composition of water can be used to better understand the complex physical and biological processes involved in land-atmosphere transport and recycling of water. The stable isotopes of hydrogen and oxygen in water vapor, precipitation, and terrestrial water sources are useful tracers of the origin and the physical and biological processes involved in the transport of water throughout the atmosphere and biosphere (Gat, 1996). The isotope composition of water vapor is related to the source of moisture, and the complex processes such as surface evaporation, atmospheric mixing and transport, moisture recycling, and cloud formation that occur throughout the life cycle of an air mass (Angert et al., 2008).

The heavy isotopes of hydrogen (^{2}H) and oxygen (^{18}O) comprise a very small fraction of natural water (approximately 0.016% and 0.2%, respectively). The isotope ratios ($^{18}O/^{16}O$, $^{2}H/^{1}H$) are affected by fractionation during phase changes. The processes of

evaporation and condensation uniquely fractionate water and leave a characteristic isotope signature. Therefore, the isotope ratios of water can be used as a tracer and as a useful diagnostic of environmental change.

Because the heavier isotopes of water exist in such small quantities, it is not useful to report them in absolute abundances. They are instead reported in their relative enrichment or depletion from a well-known standard, V-SMOW, Vienna Standard Mean Ocean Water, in parts per thousand (‰) (Eq. 1.1):

$$\delta = (\frac{R_{sample}}{R_{standard}} - 1) \times 1000 \tag{1.1}$$

where R_{sample} is the isotope ratio of D/H or $^{18}O/^{16}O$ of the sample, and $R_{standard}$ is the isotope ratio of each species of the standard (1.5576×10^{-4} for D/H and 2.0052×10^{-3} for $^{18}O/^{16}O$. Samples *enriched* relative to the standard (i.e. have a higher concentration of the heavier isotopes) are reported as positive values, and samples *depleted* in the heavy isotopes, are reported as negative values.

The fractionation processes of water isotopes are well known. Isotope fractionation occurs during phase changes as water cycles through the land and atmosphere. There are two types of fractionation: Equilibrium and kinetic. Equilibrium fractionation occurs under saturated conditions (i.e. cloud formation); therefore the amount of fractionation is determined by temperature. The equilibrium fractionation factor (α_e), is defined as (Eq. 1.2):

$$\alpha_e = \frac{R_L}{R_v} \tag{1.2}$$

where R_L is the isotope ratio of D/H or $^{18}O/^{16}O$ in liquid, and R_v is ratio of D/H or $^{18}O/^{16}O$ in vapor. The temperature dependence of (α_e) for $^{18}O/^{16}O$ and D/H has been experimentally determined by a number of investigators in the 1960's and 1970's. The results of Majoube (1971) are the most widely used:

$$^{18}O/^{16}O : \ln \alpha_{l-v} = 1137/T^2 - 0.4156/T - 0.00207 \tag{1.3}$$

$$^{2}H/^{1}H : \ln \alpha_{l-v} = 24844/T^2 - 76.248/T + 0.05261 \tag{1.4}$$

The equilibrium fractionation factor can also be expressed in delta (δ) notation: ($\epsilon_e = (\alpha_e - 1) \times 1000$). Table 1.1 shows the temperature dependence of the equilibrium fractionation factors. At standard temperature (20°C) the fractionation factors (α) for D/H and $^{18}O/^{16}O$ are 1.0852 and 1.0098 ($\epsilon_D = 85.2, \epsilon_{18}O = 9.8$), meaning that vapor in equilibrium with liquid water is depleted 85.2‰ in D and 9.8‰ in ^{18}O relative to liquid. Equilibrium fractionation factors decrease as temperatures increase, which means less fractionation occurs between liquid and vapor at higher temperatures and more fractionation occurs at lower temperatures. The ratios of $\epsilon_D/\epsilon_{18O}$ show that equilibrium fractionation is approximately 8-10 times stronger for deuterium than for oxygen-18.

Table 1.1: Equilibrium fractionation factors for 0-25°C

	Temperature °C					
Equilibrium isotope fractionation (‰)	0	5	10	15	20	25
$\epsilon_D = (\alpha_e - 1) \times 1000$	112.6	104.9	97.9	91.3	85.2	79.5
$\epsilon_{18O} = (\alpha_e - 1) \times 1000$	11.7	11.2	10.7	10.3	9.8	9.4
$\epsilon_D/\epsilon_{18O}$	9.62	9.36	9.15	8.86	8.69	8.45

Under unsaturated conditions, additional fractionation occurs and is due to the differences in the molecular diffusivities of the water molecules. This fractionation, called kinetic fractionation (α_K), is present during evaporation, and unlike equilibrium fractionation, is independent of temperature (Jouzel, 2007). Experiments by Stewart (1975) showed that relative humidity is the most important factor determining the kinetic fractionation effect. Kinetic fractionation becomes more important as relative humidity decreases.

Kinetic fractionation effects are due to the fact that the molecular diffusivity differs between the different isotopes of water. The diffusion-controlled kinetic fractionation factor has been determined to be $\alpha_K = (D_i/D_o)^n$ where D_i and D_o are the molecular diffusivities of the heavier isotopes (^{18}O or ^{2}H) and the lighter isotopes (^{16}O or ^{1}H), respectively. Experiments by Cappa et al. (2003) showed the isotope diffusivity ratios $(D_i/D_o)$to be $D_{18O}/D_{16O} = 0.9691$ and $D_D/D_H = 0.9839$. The kinetic fractionation

factor can be expressed in δ-notation (Eq. 1.5):

$$\epsilon_K = n(1 - D_i/D_o) \times 1000 \tag{1.5}$$

The exponent *n* takes the value of 1.0 for molecular diffusion (stagnant interface such as soil water or leaf water (Horita et al., 2008), 2/3 for diffusion through the laminar layer, and 0.5 under turbulent conditions (Merlivat and Jouzel, 1979; Craig and Gordon, 1965). Molecular diffusion results in a kinetic fractionation factor (ϵ_K) of 32‰ for δ^{18}O and 16.1‰ for D, resulting in kinetic fractionation that is nearly twice as strong for ^{18}O than it is for D.

A global survey by Craig (1961) showed a linear relationship between δ^{18}O and δ^{2}H in natural precipitation samples. This relationship is known as the Global Meteoric Water Line (GMWL):

$$\delta D = 8 \times \delta^{18}O + 10 \tag{1.6}$$

The slope of 8 arises from the fact that equilibrium fractionation effects are approximately 8 times stronger for D than for ^{18}O, and the y-intercept of 10 is representative of the average kinetic fractionation effects over the oceanic moisture sources (Jouzel et al., 2007). The GMWL provides a useful reference point of comparison for local and regional precipitation. The differences in a local meteoric water line (LMWL) compared with the GMWL can be interpreted based on a number of local variables including land surface cover, ET, and surface temperature.

As an air mass travels from its original source of moisture, it will become relatively

depleted as the heavier isotopes condense and precipitate first. A Rayleigh distillation model describes the evolution of the isotope ratio of a precipitating air mass (Eq. 1.7):

$$R_v = \frac{R_L}{\alpha_e}(\frac{m}{m_o})^{1/\alpha_e - 1} \tag{1.7}$$

where R_v is the isotope ratio of the vapor, R_L is the isotope ratio of the initial liquid water, α_e is the equilibrium fractionation factor, and m_o and m are the initial mass and current mass of water vapor, respectively. There are predictable patterns of precipitation that agree well with Rayleigh distillation models. Observed patterns of precipitation show relative isotopic depletion at higher latitudes, higher altitudes, and at locations farther from the coasts (Dansgaard, 1964). Air masses from different moisture sources show distinct isotopic signatures. Although this model has proven to work over relatively long time scales, it does not adequately take into account small scale processes occurring over short periods of time. A number of variables the Rayleigh distillation model does not explicitly account for are ET fluxes, boundary layer entrainment, raindrop evaporation, and others (Dansgaard, 1964).

The successive depletion of water vapor and precipitation from a moving air mass according to the Rayleigh model will conserve the slope and intercept of the meteoric water line. However, this approximation is overly simplified because it does not take into account the surface moisture fluxes along the air mass trajectory. The introduction of the deuterium excess parameter (d) (Eq. 1.8) is useful because it can identify the admixture

of continental evaporation to the original oceanic moisture source of the air mass.

$$d = \delta D - 8 \times \delta^{18}O \tag{1.8}$$

The d parameter provides information about the role of kinetic fractionation effects at the evaporative source region and along an air mass trajectory that cannot be obtained from δ D or δ^{18}O individually (Dansgaard, 1964; Merlivat and Jouzel, 1979; Gat et al., 1994; Uemura et al., 2008). The d parameter is an important diagnostic tool because it will be conserved in the air mass unless kinetic fractionation effects occur. The d does change with the evaporation of raindrops under a cloud base, or the mixture of evaporation to the advected moisture of the air mass (Gat, 2005). In the case of evaporation from falling raindrops, the remaining liquid in the drops becomes more enriched, while the d-excess parameter of the precipitation decreases. This results in a higher d in the surrounding water vapor (Jacob and Sonntag, 1991).

Any evaporative process that occurs under unsaturated conditions fractionates water in a way that alters *d*. Evaporation from soil, and water bodies, and transpiration at sub-daily timescales are non-equilibrium processes that return moisture to the atmosphere isotopically depleted in a way that results in a high *d*. This is because isotopic depletion during evaporation due to kinetic fractionation is nearly double for ^{18}O relative to ^{2}H. The d in precipitation and water vapor can therefore be used to identify continental evaporation and moisture recycling. This tool was used by Gat et al. (1994) to quantify the contribution of evaporation from the Great Lakes to atmospheric water vapor, and has been subsequently used by other researchers to identify moisture sources and recy-

cling processes (Zhang et al., 2010; Froehlich et al., 2008; Kurita and Yamada, 2008; Machavaram and Krishnamurthy, 1995).

There is considerable research on the isotopic composition of precipitation. The International Atomic Energy Agency (IAEA) and the World Meteorological Organization (WMO) have been measuring the isotopic composition of precipitation since 1961. These data have been compiled into a database known as the GNIP (Global Network of Isotopes in Precipitation) (IAEA-WMO, 2006). The spatial and temporal characteristics of global precipitation in GNIP has been well summarized by Rozanski et al. (1993) and confirmed many of the early findings of Dansgaard (1964). Currently, many of the GNIP stations are not updated; however, Welker (2000) analyzed precipitation sampled collected by the National Atmospheric Deposition Program (NADP) network across the United States, and determined they are suitable for contribution to GNIP.

The isotope composition of precipitation samples integrates the meteorological processes and fractionation effects that occur over the lifetime of that air mass. While isotopic measurements of precipitation can provide information about the moisture source, atmospheric mixing, and the contribution of local evaporative processes to the precipitating air mass, precipitation itself is sporadic, relatively unpredictable, and may not be frequent enough to resolve moisture transport questions that occur on smaller or shorter scales. A major advantage of measuring water vapor isotopes is the ability to measure across a range of atmospheric conditions, since measurements are not limited to rainy days.

Compared with the extensive network of precipitation isotope measurements, relatively few researchers have measured the isotope composition of water vapor. Previously, flask-

sampling of water vapor was used for the collection of water vapor for isotopic analysis (e.g. (Jacob and Sonntag, 1991; He and Smith, 1999; Yamanaka and Shimizu, 2007; Angert et al., 2008)). Recent advances in laser-based technologies have been made that allow near-continuous measurements of water vapor isotopes possible (Lee et al., 2005; Gupta et al., 2009; Iannone et al., 2010; Griffis et al., 2010b), and these types of measurements are on the verge of becoming routine at many research sites.

In order to fully utilize the tracer capacity of the isotope ratios of hydrogen and oxygen in water vapor, precipitation, and surface water sources, and the potential of these species to help predict future change, we must first understand how these species relate to the current meteorological and climatological conditions. In addition, the influence of changing surface characteristics on the isotope ratios of surface layer air must be understood. This thesis utilizes direct measurements of δ^{18}O and δ^{2}H in water vapor on a tall tower in Rosemount, MN, in conjunction with measurements of the isotopic composition of precipitation and terrestrial water pools, to develop a landscape-scale understanding of the controlling mechanisms of the isotope ratios of water vapor in the atmospheric boundary layer. This comprehensive analysis helps us gain insight into the important processes involved in the local and large-scale transport of water and help diagnose environmental and hydrological change.

The first chapter of this thesis addresses a methodological problem related to the isotope analysis of water extracted from plant and soil samples. Spectral interference caused by organic compounds present in plant and soil waters has excluded the use of isotope ratio infrared spectroscopy (IRIS) analyzers in the isotope analysis of of plant and soil waters.

Here, a correction method was conducted and compared to the isotope ratios measured using isotope ratio mass spectrometry (IRMS). The correction method eliminated the discrepancies between IRMS and IRIS for δ^{18}O, and greatly reduced the discrepancies for δ^{2}H. In fact, the discrepancies in δ^{2}H may potentially be due to contamination problems using IRMS, not IRIS (personal communications with Los Gatos Research, Inc). This procedure shows that it is possible to use IRIS analyzers for the isotope analysis of plant and soil samples.

The second chapter of this thesis addresses the variations in the isotope composition of water vapor in the atmospheric boundary layer, and the important mechanisms involved in controlling these variations. Measurements of δ^{18}O and δ^{2}H in water vapor were continuously measured at two heights on the tall tower in Rosemount, MN from May, 2010 through June, 2011. Observed variations in δ^{18}O, δ^{2}H, and *d* in water vapor were caused by a combination of Rayleigh rainout effects, atmospheric dynamics, and surface influences.

Chapter 2

Identification and correction of spectral contamination in $^{2}H/^{1}H$ and $^{18}O/^{16}O$ measured in leaf, stem, and soil water

Chapter Summary

Plant water extracts typically contain organic materials that may cause spectral interference using isotope ratio infrared spectroscopy (IRIS), resulting in errors in the measured isotope ratios. IRIS manufacturers have developed post-processing software to identify the degree of contamination in water samples, and potentially correct the isotope ratios of water with known contaminants. Here, the correction method proposed by IRIS manufacturer, Los Gatos Research, Inc., was conducted and compared to isotope ratio mass spectrometry (IRMS). Deionized water was spiked with methanol and ethanol to create correction curves for δ^{18}O and δ^{2}H. The contamination effects of different sample types (leaf, stem, soil) and different species from agricultural fields, grasslands, and forests were compared. The average corrections in leaf samples ranged from 0.35 to 15.73‰ for δ^{2}H and 0.28 to 9.27‰ for δ^{18}O. The average corrections in stem samples ranged from 1.17 to 13.70‰ for δ^{2}H and 0.47 to 7.97 for δ^{18}O. There was no contamination observed in soil water. Cleaning plant samples with activated charcoal had minimal effects on the degree of spectral contamination, reducing the corrections, on average, 0.44‰ for δ^{2}H and 0.25‰ for δ^{18}O. The correction method eliminated the discrepancies between IRMS and IRIS for δ^{18}O, and greatly reduced the discrepancies for δ^{2}H. The mean differences in isotope ratios between IRMS and corrected IRIS methods were 0.18‰ for δ^{18}O, and -3.39‰ for δ^{2}H. The inability to create an ethanol correction curve for δ^{2}H likely caused the larger discrepancies. We conclude that ethanol and methanol are the primary compounds causing interference in IRIS analyzers, and that each individual analyzer will likely require custom correction curves.

2.1 Introduction

Stable isotope analyses of plant and soil water are routinely performed, and have been used to better understand water use patterns in terrestrial ecosystems (West et al., 2007; Lee et al., 2007),to partition the components of evapotranspiration (Yakir and Wang, 1996; Williams et al., 2004; Wang et al., 2010), and to understand the controls on surface H_2O and CO_2 fluxes (Lee et al., 2007; Welp et al., 2008; Lai and Ehleringer, 2011; Griffis et al., 2011). In the past, the analysis of $^{18}O/^{16}O$ and $^{2}H/^{1}H$ in liquid water has been exclusively conducted using stable isotope ratio mass spectrometry (IRMS). Recently, the development of isotope ratio infrared spectroscopy (IRIS) has simplified the isotope analysis of water, allowing the simultaneous measurement of $^{18}O/^{16}O$ and $^{2}H/^{1}H$ in liquid water. Isotope ratio infrared spectroscopy analyzers do not require the chemical conversion of compounds to their elemental constituents prior to analysis unlike IRMS. Additional benefits of IRIS analyzers include cost, speed of analysis, and portability (Gupta et al., 2009).

The analytical precision and accuracy of IRIS analyzers are similar to that of IRMS when analyzing pure water (Gupta et al., 2009; Brand et al., 2009); however, it has recently been shown that there are discrepancies between the isotope ratios of plant and soil water measured with IRIS and IRMS (Brand et al., 2009; West et al., 2010). The conventional method of cryogenic vacuum distillation (e.g West et al., 2006) for extraction of water from plant and soil samples can co-distill organic materials (e.g. methanol and ethanol) that may interfere with the spectral signal for the IRIS methods, resulting in erroneous isotope values. Research by West et al. (2010) found deviations as large as

46.5‰ and 15.4‰ for δ^2H and δ^{18}O, respectively from water extracted from a range of 12 plant and soil samples collected in or near Berkeley, CA, USA. The effect of cleaning the samples with activated charcoal reduced, but did not eliminate the deviations, since activated charcoal is inefficient in removing alcohols, glycols, strong acids, and bases (Brand, 2010).

In response to the observed spectral interference by organic materials in plant and soil samples, IRIS manufacturers (Los Gatos Research Inc., Picarro Inc.) have developed software to identify and quantify the presence of contaminants in water samples. Here, we use the Liquid Water Isotope Analyzer (LWIA) (DLT-100) from Los Gatos Research Inc. with the Spectral Contamination Identifier (LWIA-SCI) post-processing software to identify and quantify spectral contamination, and correct the isotope values of contaminated water samples. The instrument manufacturer has proposed a method to correct the isotope ratios of contaminated samples if the contaminants are known. The correction method consists of spiking clean water with known contaminants and measuring the degree of contamination based on the output from the LWIA-SCI software. In this study, we test how well this correction method works. To our knowledge, this is the first study to attempt to correct the isotope ratios in plant and soil samples with known contamination with an IRIS analyzer.

The objectives of this study are to (1) quantify the measurement errors of $^{18}O/^{16}O$ and $^{2}H/^{1}H$ associated with spectral interference caused by organic contaminants, (2) compare the contamination effects of different sample types (leaf, stem, soil) and species from agricultural fields, grasslands, and forests, (3) correct the isotope ratios of contaminated

water samples, and (4) test the accuracy of the corrections by comparing the results to the traditional IRMS technique.

2.2 Materials and Methods

2.2.1 Sample collection and isotope analysis

Leaf, stem, and soil samples were collected from the (1) Rosemount Research and Outreach Center (RROC) in Rosemount, MN, USA, approximately 25 km southeast from Minneapolis (Griffis et al., 2010a), (2) the Marcell Experimental Forest (MEF) in northern Minnesota (Shurpali and Verma, 1998), and (3) the Borden Forest Research Station (BFRS) in southern Ontario, Canada (Lee et al., 1999; Kim, 2011). Table 1 shows the plant species included in this study. No other study has examined the contamination effects of these species.

Following the sampling protocol given by the Moisture Isotopes in the Biosphere and Atmosphere (MIBA) program (http://www-naweb.iaea.org/napc/ih/IHS_resources_miba.html), we collected leaf, stem, and soil samples near midday (12:00 local standard time (LST)). Dry, healthy sunlit leaves were chosen for analysis. If a distinct major vein was visible, it was removed and discarded. Non-green stem samples were collected at the base of the plants. Soil samples were collected from approximately 10 cm below the soil surface. All samples were sealed in glass vials with parafilm, and frozen until water extraction on a custom made vacuum glass line.

Cryogenic vacuum distillation (West et al., 2006) was used to extract water from the

plant and soil samples. During the process of vacuum distillation, water is evaporated from the plant or soil sample and frozen in a collection tube. Complete water extraction was ensured to avoid isotope fractionation. Plant and soil samples were weighed post-extraction, oven-dried, and weighed again. The oven-drying process was assumed to completely dry the sample. If there was a discrepancy between the post-extraction mass and oven-dried mass of a sample, the sample was discarded. During this process, organic compounds within plant cells may co-distill with the water, causing spectral contamination using IRIS. Each sample was pipetted into a small vial, sealed with parafilm, and refrigerated until isotope analysis. Individual plant samples with sufficient water for duplicate analyses were divided into two sub-samples to test the effect of activated charcoal on the spectral contamination. Following West et al. (2010), activated charcoal was added in excess of 10% of the total mass of the sample and mixed well. After a minimum of 24 hours, the samples with activated charcoal were filtered using a 0.45m filter into new vials.

The isotope analysis of all liquid water extracted from plant and soil samples was performed on a Liquid Water Isotope Analyzer (DLT-100, Los Gatos Research, Inc., Mountain View, California) coupled to an autosampler (HT-300A, HTA s.r.l., Brescia, Italy) at the Biometeorology Lab at the University of Minnesota. Manufacturer specifications give a precision of 1.0‰ for δ^2H and 0.25‰ for δ^{18}O. The LWIA calculates the spectral absorbance of $^2H/^1H$ and $^{18}O/^{16}O$ at infrared wavelengths using off-axis integrated cavity output spectroscopy (OA-ICOS). Because the analyzer measures the concentrations of the individual isotopoloques and reports them in absolute ratios, it is necessary to include pre-

calibrated internal laboratory standards within and throughout the autoruns to calibrate the unknown samples to Vienna Standard Mean Ocean Water (VSMOW). Standards for each autorun are selected based on the expected isotopic composition of the unknown samples and should bracket the range of unknown samples. Linear calibration equations are calculated using each set of standards throughout the run and used to correct unknown samples. All measured unknown water samples are calibrated to the known internal water standards and reported in delta (δ) notation relative to VSMOW [$\delta = (R_{sample}/R_{VSMOW}$ - 1) $\times$ 1000] where R_{sample} is the isotope ratio (e.g. $^{18}O/^{16}O$) of the sample, and R_{VSMOW} is the isotope ratio of the standard, VSMOW. The standard deviation of the water standards throughout a typical autorun is better than 0.8‰ for δ^2H and 0.3‰ for $\delta^{18}O$, and is typically around 0.4‰ for δ^2H and 0.1‰ for $\delta^{18}O$.

2.2.2 Contamination identification and correction

If other compounds are present in the water samples that absorb in the same wavelengths used to detect the isotopes of hydrogen and oxygen, errors in the measured ratios of $^2H/^1H$ and $^{18}O/^{16}O$ may occur. It has been shown that organic molecules present in water extracted from plants interfere with the spectral signal using IRIS approaches, and can produce significant errors in the measured isotope ratios (Brand et al., 2009; West et al., 2010). Only molecules with similar absorption features in the same spectral region that also have an O-H bond will likely interfere with the measured $^2H/^1H$ and $^{18}O/^{16}O$ ratios (Brand, 2010). Therefore, the most likely compounds causing contamination are methanol (MeOH) and ethanol (EtOH).

The LWIA Spectral Contamination Identifier (LWIA-SCI) software was developed by Los Gatos Research Inc. to identify features in the LWIA spectra that are consistent with water contamination. Briefly, the recorded spectra from unknown samples are analyzed and compared to known clean samples (such as standards) to produce a metric of contamination from either narrow-band (e.g. MeOH) or broad-band (e.g. EtOH) absorbers. The metric of contamination indicates the likelihood or degree of spectral interference. If the contaminant(s) are known, it should be possible to correct the isotope ratios of contaminated samples based on the magnitude of the metric of contamination.

In order to correct the isotope ratios of contaminated samples, deionized (DI) water was spiked with varying amounts of EtOH and MeOH to measure the isotope errors associated with the magnitude of the contamination metric. The approximate range of EtOH and MeOH concentrations used to create these correction curves was 0.5% to 5.0%, and 45 ppmv to 0.2%, respectively. Based on these relationships, correction curves were derived to adjust the measured isotope ratio of water samples with varying degrees of contamination. Figure 1 presents the change in δ^{18}O and δ^{2}H with the addition of EtOH. There was a clear linear relationship between the broad-band (BB) metric and the offset in δ^{18}O given by Eq. 1:

$$BB = -0.1653 \times \Delta\delta^{18}O - 0.9749 \tag{2.1}$$

Unfortunately, there was no clear relationship between $\Delta\delta^{2}$H and the BB metric; therefore it was not possible to correct δ^{2}H in samples with broad-band contamination.

Figure 2 presents the change in δ^{18}O and δ^{2}H with the addition of MeOH. Because the

size of a MeOH molecule is more similar than EtOH to a water vapor molecule, it has a stronger effect on the measured isotope ratios.[10] To best describe the offset in δ^2H and δ^{18}O over the full range of contamination, two separate equations were used. Eqs. 2a and 2b describe the relationship between the NB metric and δ^2H at the NB metric $\leq$ 4000 and 4000 respectively:

$$NB_{\leq 4000} = 27.3 \exp\left(0.3541 \times \Delta\delta^2 H\right) - 27.3 \quad \text{(2.2a)}$$

$$NB_{>4000} = 528.9 \exp\left(0.1699 \times \Delta\delta^2 H\right) - 528.9 \quad \text{(2.2b)}$$

Eqs. 3a and 3b describe the relationship between the NB metric and δ^{18}O$\leq$ 4000 and 4000 respectively:

$$NB_{\leq 4000} = 15.67 \exp\left(0.716 \times \Delta\delta^{18} O\right) - 15.67 \quad \text{(2.3a)}$$

$$NB_{>4000} = 645.6 \exp\left(0.2612 \times \Delta\delta^{18} O\right) - 645.6 \quad \text{(2.3b)}$$

The LWIA-SCI software outputs the NB or BB metric for each individual sample. Based on those metrics, Eqs. 1-3 were used to solve for δ^{18}O and δ^2H. The MeOH and EtOH equations corrected the isotope ratios in different directions. The addition of MeOH to DI water resulted in more positive isotope values, and the corrections needed to be subtracted from the original isotope values, while the addition of EtOH to DI water resulted in more negative isotope values, and the corrections needed to be added

to the original isotope values. In samples with both NB and BB contamination, both correction curves (δ^{18}O only) were used to adjust the isotope ratios of the samples. In these instances, each correction curve was applied to the original value of δ^{18}O, the NB and BB corrections were summed, and the final correction was used to adjust δ^{18}O.

2.2.3 IRMS analysis and comparison

The IRIS values of the 78 leaf samples from the Borden Experimental Forest were compared to IRMS values in a blind comparison to test the accuracy of the correction method. In the blind comparison, the IRMS values were not known prior to applying the corrections to the IRIS analyzed isotope values. The CO_2 equilibration method was used to determine the δ^{18}O values of the leaf water samples (mass-spectrometer model DeltaPlus XP with Gas Bench, Thermo Finnigan, Cambridge, UK.) The δ^{2}H values were determined using a chromium reaction (mass spectrometer model Thermo Finnigan MAT 253 with an H-device) at Yale University (Kim, 2011). Precision was 0.2‰ for δ^{18}O and 1.0‰ for δ^{2}H.

2.2.4 Statistical analysis

To assess the significance of the difference between the uncorrected and corrected IRIS measurements, the uncorrected and corrected IRIS measurement results were compared using one-way ANOVA for both δ^{2}H and δ^{18}O at the 95% significance level ($\alpha = 0.05$ level) for each species and sample type. The p-values are reported in Table 2. To determine whether the addition of activated charcoal to plant water samples prior to analysis had significant effects on the final corrected isotope ratios, the final isotope

ratios of the samples with and without activated charcoal added were compared using one-way ANOVA at an $\alpha = 0.05$ level. The p-values are reported in Table 3.

2.3 Results

2.3.1 Contamination and correction

Figure 3 presents the average corrections by species and sample type. The error bars represent the 95% confidence interval. All of the plant species exhibited some degree of spectral contamination. No contamination was observed in the soil samples (Table 2). The average corrections for stem samples among the species analyzed ranged from 1.17 to 13.70‰ for δ^2H and 0.47 to 7.97‰ for δ^{18}O. The lowest average corrections were observed in corn and leather leaf for δ^{18}O and δ^2H, respectively, with the highest average corrections observed in clover. The maximum correction in a stem sample was 34.63‰ for δ^2Hand 20.83‰ for δ^{18}O (clover). The average corrections for leaf samples ranged from 0.35 to 15.73‰ for δ^2H and 0.28 to 9.27‰ for δ^2H. The lowest average corrections were observed in big bluestem and the highest average corrections were observed in greater creeping spearwort. The maximum correction in a leaf sample was 34.76‰ for δ^2H and 20.94‰ for δ^{18}O (soybean). Statistically significant differences between the uncorrected and corrected IRIS mean δ^{18}O values were observed in soybean leaves, clover leaves, spearwort leaves, white ash leaves, soybean stems, clover stems, and cotton grass stems. In the mean δ^2H values, statistically significant differences were observed in white ash leaves and clover stems. It is important to note that because of the large variations in

contaminant levels within species, each sample needed to be corrected individually, not as a blanket correction factor for each species.

According to West et al. (2010), leaf water typically contains a higher fraction of organic contaminants than water extracted from stems. This was not necessarily the case with our samples. For corn, spearwort, and leather leaf, there was more contamination observed in the leaves than in the stems. On the other hand, for soybean, big bluestem, clover, and cottongrass, there was more contamination observed in the stems than in the leaves. For the two grasses sampled (big bluestem and cottongrass), the errors in the stems were notably higher than the errors in the leaves.

2.3.2 Effect of activated charcoal

Cleaning plant samples with activated charcoal had minimal effects on the degree of spectral contamination observed in leaf and stem samples. Table 3 presents a summary of the isotope ratios and correction values for samples treated with and without activated charcoal. With the exception of one sample (big bluestem stem), activated charcoal reduced the average corrections from 9.72‰ to 9.28‰ for δ^2H, and from 5.61‰ to 5.36‰ for δ^{18}O, resulting in average correction reductions of 0.44‰ and 0.25‰ for δ^2H and δ^{18}O, respectively. Inexplicably, the activated charcoal removed all contamination from a big bluestem stem sample. Comparing the cleaned and uncleaned samples, the final isotope values of this stem sample agree well, with a small difference of 0.19‰ in δ^2H and 0.51‰ in δ^{18}O. Overall, there were small differences between the final values of δ^{18}O and δ^2H in cleaned and uncleaned samples, with an average difference of 0.33‰ for δ^2H, and

0.42‰ for δ^{18}O. None of these differences were statistically significant. These results suggest that the main contaminants in plant samples are in fact methanol and ethanol, although other contaminants were removed with activated charcoal (big bluestem stem). We conclude that the process of cleaning plant samples with activated charcoal has minimal effects on this correction procedure. The use of activated charcoal produces a cleaner sample however, and it is good laboratory practice to use activated charcoal because of the potential negative effects of injecting impure water samples into the analyzer (i.e. memory effects, clogged filters, sample cell integrity) (Brand, 2010).

2.3.3 Comparison with IRMS

The accuracy of the correction method was tested by comparing the corrected IRIS isotope ratios of leaf samples with the isotope ratios of the same samples analyzed using IRMS in a blind comparison. The 78 leaf samples–from white ash, large tooth aspen, red maple–from the Borden Experimental Forest were used in this comparison. We assume that δ^{18}O and δ^{2}H measured via IRMS represent the "true" isotope values of the leaf samples (West et al., 2010). Figure 4 presents the comparison of δ^{18}O and δ^{2}H in leaves measured with IRMS and the corrected IRIS methods. Overall, the isotope corrections eliminated the discrepancies between δ^{18}O measured using IRIS and IRMS and greatly reduced the discrepancies in δ^{2}H. The mean difference in isotope ratios between IRMS and (corrected) IRIS methods (δ_{IRMS} - δ_{IRIS}) was 0.18‰ for δ^{18}O and -3.39‰ for δ^{2}H. Without the IRIS correction, the mean differences between IRMS and IRIS were -3.06‰ for δ^{18}O and -8.98‰ for δ^{2}H, and as large as -12.84‰ and -28.24‰ for δ^{18}O and δ^{2}H, respectively.

We further investigated the offset in δ^2H by analyzing a pure water sample using the same IRIS and IRMS methods to determine if the offset resulted from a bias caused by different water standards used in the Yale University and University of Minnesota labs. The isotope values of this water sample, based on 10 replicated samples using the IRIS method, were -122.6 0.7‰ for δ^2H, and -16.34 0.24‰ for δ^{18}O. The isotope values of this sample, based on 12 replications using the IRMS methods, were -123.5 0.4‰ for δ^2H, and -16.39 0.07‰ for δ^{18}O. There was excellent agreement between the two methods on the pure water sample (a difference of 0.94‰ for δ^2H and 0.05‰ for δ^{18}O), eliminating instrument bias as a cause of the δ^2H offset.

2.4 Discussion and Conclusions

Using the proposed correction method, we were able to eliminate the errors in δ^{18}O nd greatly reduce the errors in δ^2H caused by spectral contamination. We suspect that the incomplete corrections in δ^2H resulted from the inability to create a correction curve for ethanol contamination. There was no clear relationship between $\Delta\delta^2$H and the broad-band contamination metric (see Figure 1). The offset could also be due to the interference of other contaminants. The accuracy of the corrected δ^{18}O values confirms the fact that ethanol and methanol are the primary contaminants causing spectral interference; however, additional contaminants may have been removed with activated charcoal.

In theory, these correction curves should be applicable to water samples analyzed on other LGR water isotope instruments. However, when comparing our correction curves with the example curves created by LGR in their SCI-LWIA manual, large differences are

evident in both magnitude and direction of the corrections. Thus, it is likely that each individual analyzer will require custom made correction curves. Further research is required to evaluate if these correction curves are stable over time.

According to the comparison of the IRIS and IRMS analyzed Borden Experimental Forest leaves, this correction method has an accuracy of -3.39‰ for δ^2H and 0.18‰ for δ^{18}O. The standard deviation of the differences (IRMS - IRIS corrected) was 1.98‰ and 0.58‰, respectively, which includes measurement noise in both instruments. We can conclude that the overall precision of the IRIS method with corrections is better than 1.98‰ for δ^2H, and 0.58‰ for δ^{18}O. It is important to note that not all species analyzed in this study by IRIS methods were compared to IRMS measurements. It is therefore too soon to conclude that these correction curves will have the same accuracy and precision across all species. We recommend that the corrected values of each individual species are validated against traditional IRMS methods for complete confidence in these methods, and that the correction curve data (e.g. equations, R^2 values, range of contaminant levels) are reported for each individual analyzer.

Recently, West et al. (2011) recommended that the use of spectral contamination identification software become incorporated into IRIS standard data post-processing protocols to ensure data quality. We agree with this recommendation, but disagree with their conclusion to discard all contaminated IRIS data. Instead, we recommend following our protocol of creating correction curves for known contaminants, and validating the corrected isotope values of new species or sample types against IRMS methods.

It should be noted that the correction curves in this experiment were created based on

the degree of contamination observed in the plant water samples. In our plant samples, the maximum corrections were 34.76‰ for δ^2H and 20.94‰ for δ^{18}O. Recently, Zhao et al. (2011) reported errors in IRIS measurements as large as 224‰ for δ^2H for some species. We have not investigated the accuracy of these particular correction curves at higher contamination levels.

There have been no instances of contamination using optical techniques to conduct in situ measurements of δ^2H and δ^{18}O in water vapor (Lee et al., 2005; Griffis et al., 2010b). This is likely a non-issue because concentrations of potential contaminants are very low in the atmosphere (e.g. MeOH concentration is 2 parts per billion (ppb) in the winter, and 7 ppb in the summer at the RROC Trace Gas Observatory) (Hu et al., 2011). The atmospheric MeOH concentrations are an order of magnitude less than the minimum amounts observed to cause spectral contamination on the liquid water analyzer.

In conclusion, we showed that it is possible to correct δ^2H in plant water extracts that contain organic contaminants that cause spectral interference using IRIS. We used a liquid water isotope analyzer with spectral contamination identifier post-processing software to identify and quantify contamination in water samples. Correction curves for δ^{18}O and δ^2H were created by spiking DI water with known contaminants, methanol and ethanol. It was possible to correct δ^{18}O for methanol and ethanol contamination, but it was only possible to correct δ^2H for methanol contamination. We analyzed water extracted from leaf, stem, and soil samples and found spectral contamination in all plant species, and no contamination in soil water. We compared our corrected IRIS measurements of leaf samples to IRMS measurements of the same samples and found exceptional agreement

in δ^{18}O of 0.18‰, within the margin of error of the instrument. There was a difference of -3.39‰ between the IRMS and IRIS methods, likely due to the inability to correct for ethanol contamination for δ^{2}H. There is significant potential to use IRIS methods to analyze water extracted from leaves and stems; however, IRMS methods are still needed for IRIS quality validation, and it is likely that the correction curves may vary among instruments. Until an analytical solution is developed to remove all sample contaminants prior to injection in IRIS analyzers, we believe that this correction method presents a viable alternative to traditional IRMS methods for analyzing the isotope ratios of plant and soil waters.

Acknowledgments

We express our sincere thanks to Jeremy Smith for his technical assistance in the lab, Joel Fassbinder for his assistance in collecting plant and soil samples from the RROC, Donna M. Olsen for collecting plant samples from the MEF, and Kyounghee Kim for the collection and analysis of leaf water samples from the BFRS. We also thank three anonymous reviewers for their thoughtful comments and criticisms that helped improve the quality of this paper. Funding for this research has been provided by the National Science Foundation, ATM-0546476 (TG), ATM-0914473 (XL), DEB-0514908 (XL and TG), the Office of Science (BER) U.S. Department of Energy, DE-FG02-06ER64316 (TG and JB) and the College of Food, Agricultural and Natural Resource Sciences, at the University of Minnesota.

Common name	Species	Sample type
Corn	*Zea mays*	leaf, stem, soil
Soybean	*Glycine max*	leaf, stem, soil
Big bluestem	*Andropogon gerardii*	leaf, stem, soil
Purple clover	*Trifolium pretense*	leaf, stem
Creeping spearwort	*Ranunculus flammula*	leaf, stem
Snap peas	*Pisum sativum*	leaf, soil
Cotton grass	*Eriophorum chamissonis*	leaf, stem
Leather leaf	*Chamaedaphne calcyculata*	leaf, stem
White ash	*Fraxinus americana*	leaf
Large-tooth aspen	*Populus grandidentata*	leaf
Red maple	*Acer rubrum*	leaf

Table 2.1: The different plant species examined in this study. Corn, soybean, big bluestem, purple clover, and creeping spearwort samples were collected from the RROC, cotton grass and leather leaf samples were collected from the MEF, and white ash, large-tooth aspen, and red maple samples were collected from the BFRS. No other study has examined the contamination effects of these species.

Table 2.2: Contamination effects by species/sample type. The second column (n) refers to the total number of samples. The third column (# cont.) refers to the number of contaminated samples. All values are reported in per mil (‰). The p-values shown in bold are significant at the 95% confidence level.

			Before correction		$\Delta\delta^2$H	$\Delta\delta^{18}$O	*After correction*	
sample type	n	# cont.	mean δ^2H	mean δ^{18}O	mean (max) **sdev**	mean (max) **sdev**	mean δ^2H	mean δ^{18}O
corn leaf	26	22	-28.41	+5.87	3.68 (11.97) **3.61**	1.98 (5.79) **1.80**	-32.09	+3.88
soybean leaf	25	23	-20.48	+7.19	6.03 (34.76) **8.61**	3.45 (20.94) **5.01**	-26.50	+3.73
big bluestem leaf	7	4	-43.95	-1.94	0.35 (0.83) **0.32**	0.28 (0.65) **0.25**	-44.24	-2.22
clover leaf	7	7	-11.14	+10.61	11.76 (27.27) **11.87**	6.59 (15.65) **6.71**	-22.89	+4.02
spearwort leaf	5	5	-11.54	+11.18	15.73 (24.47) **11.51**	9.27 (18.08) **6.93**	-27.26	+1.91
snap pea leaf	3	3	-37.02	+7.47	13.84 (25.54) **11.26**	7.85 (14.32) **6.14**	-50.86	-0.38
cotton grass leaf	14	5	-51.57	-1.35	2.48 (6.41) **3.18**	1.13 (2.67) **1.35**	-54.05	-2.49
leather leaf leaf	14	3	-49.77	+1.61	2.65 (7.65) **4.33**	1.43 (4.04) **2.26**	-52.42	+0.18
white ash leaf	26	26	-23.07	+13.71	14.81 (23.46) **4.62**	8.84 (14.18) **2.42**	-37.88	+4.90
lg. tooth aspen leaf	26	26	-35.90	+5.37	0.90 (3.47) **0.94**	0.56 (1.91) **0.54**	-36.80	+4.81
red maple leaf	25	25	-32.79	+8.99	0.44 (1.66) **0.43**	0.26 (0.94) **0.25**	-33.23	+8.73
corn stem	7	7	-51.04	-6.27	1.77 (4.94) **1.54**	0.47 (3.11) **1.69**	-52.81	-6.73
soybean stem	10	9	-47.90	-2.27	7.07 (28.11) **8.70**	4.27 (17.24) **5.29**	-54.97	-6.54
big bluestem stem	8	3	-56.46	-4.49	6.62 (10.17) **5.52**	3.81 (5.79) **3.12**	-63.08	-8.30
clover stem	9	9	-40.27	+1.33	13.70 (34.63) **12.87**	7.97 (20.83) **7.54**	-53.97	-6.64
spearwort stem	7	7	-48.16	-1.72	7.82 (20.91) **7.74**	4.22 (11.93) **4.26**	-55.44	-5.94
cotton grass stem	15	14	-64.97	-5.70	6.36 (18.84) **6.40**	3.45 (10.66) **3.52**	-71.34	-9.15
leather leaf stem	14	2	-60.23	-6.20	1.17 (2.13) **1.37**	0.55 (1.10) **0.77**	-61.40	-6.75
soil	45	0	-51.50	-5.70	x	x	-51.50	-5.70

Table 2.3: The effects of activated charcoal on the degree of spectral contamination observed–all samples treated with activated charcoal are shown in parentheses. All values are reported in per mil (‰).

	Before correction				*After correction*	
sample type (AC)	mean δ^2H	mean δ^{18}O	$\Delta\delta^2$H	$\Delta\delta^{18}$O	mean δ^2H	mean δ^{18}O
corn leaf	-29.19 (-28.09)	+6.35 (+6.44)	4.96 (4.58)	2.59 (2.44)	-33.15 (-32.67)	+3.76 (+4.00)
corn stem	-51.43 (-51.04)	-6.07 (-6.14)	2.19 (1.95)	1.00 (0.91)	-53.62 (53.00)	-7.07 (-7.05)
big blue stem	-51.02 (-60.26)	-2.75 (-7.66)	9.43 (0)	5.42 (0)	-60.45 (-60.26)	-8.17 (-7.66)
clover stem	-36.67 (-36.88)	+2.91 (+2.62)	16.41 (15.88)	9.41 (9.14)	-53.08 (-52.76)	-6.49 (-6.51)
soybean leaf	-6.80 (-6.81)	+14.28 (+13.11)	15.80 (15.24)	9.41 (9.13)	-22.59 (-22.06)	+4.86 (+3.98)
soybean stem	-47.90 (-48.25)	-0.98 (-2.09)	9.23 (8.74)	5.66 (5.39)	-57.13 (-56.99)	-6.64 (-7.49)

Figure 2.1: The ethanol correction curves for δ^{18}O (top) and δ^{2}H (bottom). Ethanol was added to deionized water, resulting in a linear relationship between the broad-band (BB) contamination metric from the LWIA-SCI software and the offset in δ^{18}O ($\Delta\delta^{18}$O) ($BB = -0.1653 * x + 0.9749$). There was no clear relationship between the BB contamination metric and the offset in δ^{2}H ($\Delta\delta^{2}$H).

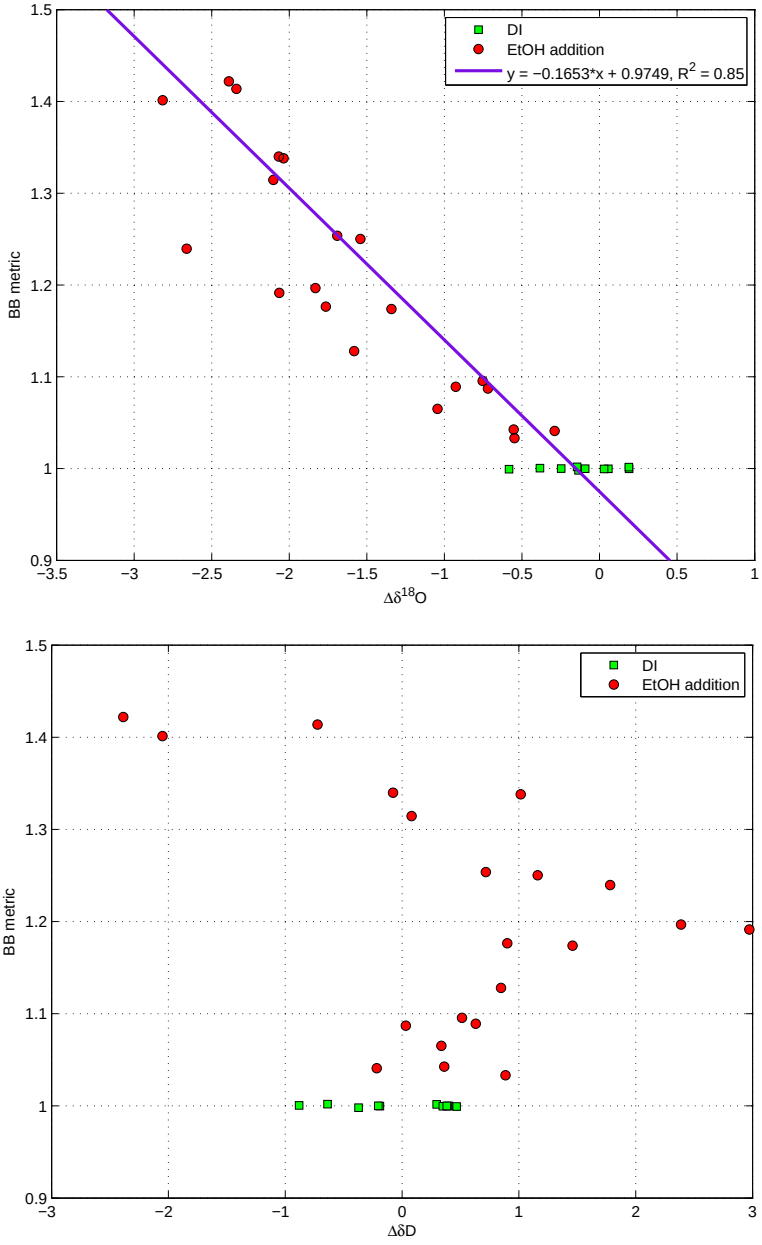

Figure 2.2: The methanol correction curves for δ^{18}O (top) and δ^{2}H (bottom). Methanol was added to deionized water to create relationships between the narrow-band (NB) contamination and the offsets in δ^{18}O and δ^{2}H. To best describe the offset in δ^{2}H and δ^{18}O over the full range of contamination, two separate equations were used for δ^{18}O and δ^{2}H. For δ^{18}O, $NB_{\leq 4000} = 15.67 \exp(0.716 \times \Delta\delta^{18}O) - 15.67$ and $NB_{>4000} = 645.6 \exp(0.2612 \times \Delta\delta^{18}O) - 645.6$. For δ^{2}H, $NB_{\leq 4000} = 27.3 \exp(0.3541 \times \Delta\delta^{18}O) - 27.3$ and $NB_{>4000} = 528.9 \exp(0.1699 \times \Delta\delta^{18}O) - 528.9$.

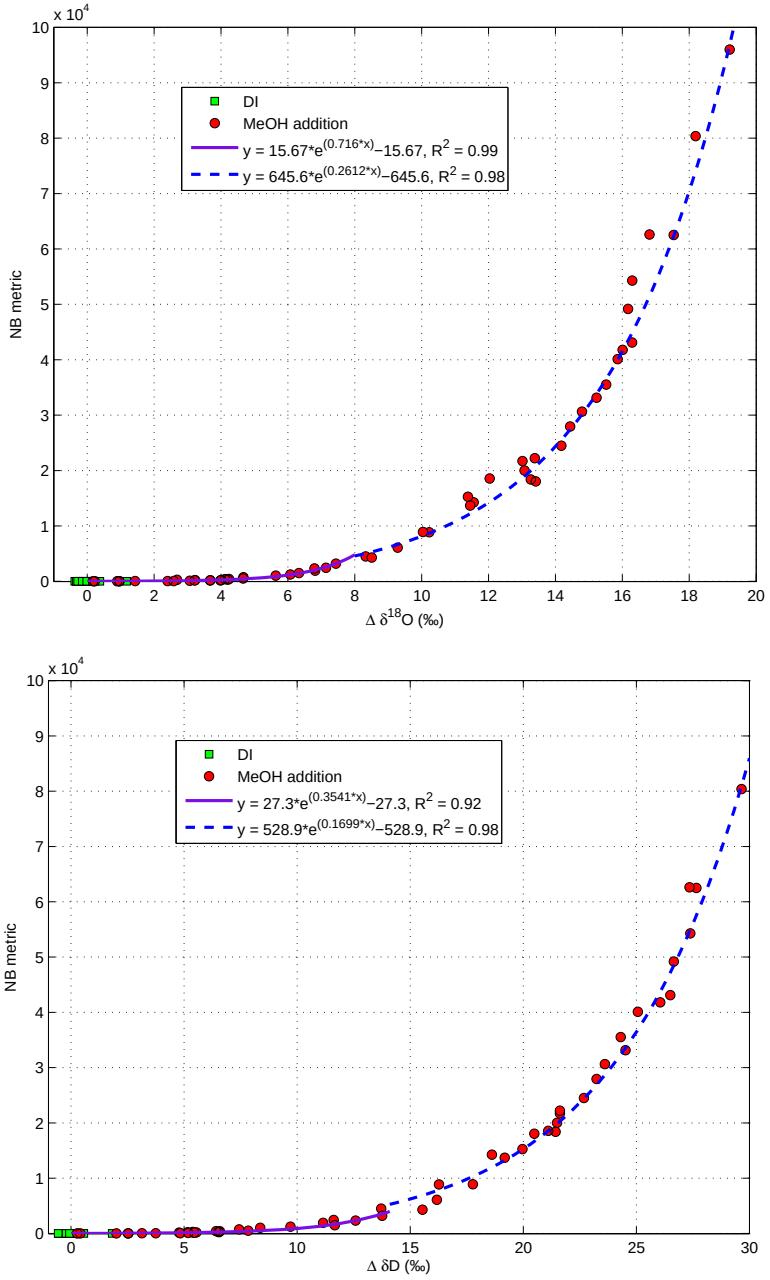

Figure 2.3: The average corrections for the leaf and stem samples analyzed. The error bars represent the 95% confidence interval. The average corrections in leaf samples ranged from 0.35 to 15.73‰ for δ^2H and 0.28 to 9.27‰ for δ^{18}O. The average corrections in stem samples ranged from 1.17 to 13.70‰ for δ^2H and 0.47 to 7.97‰ for δ^{18}O. There was no contamination observed in soil water.

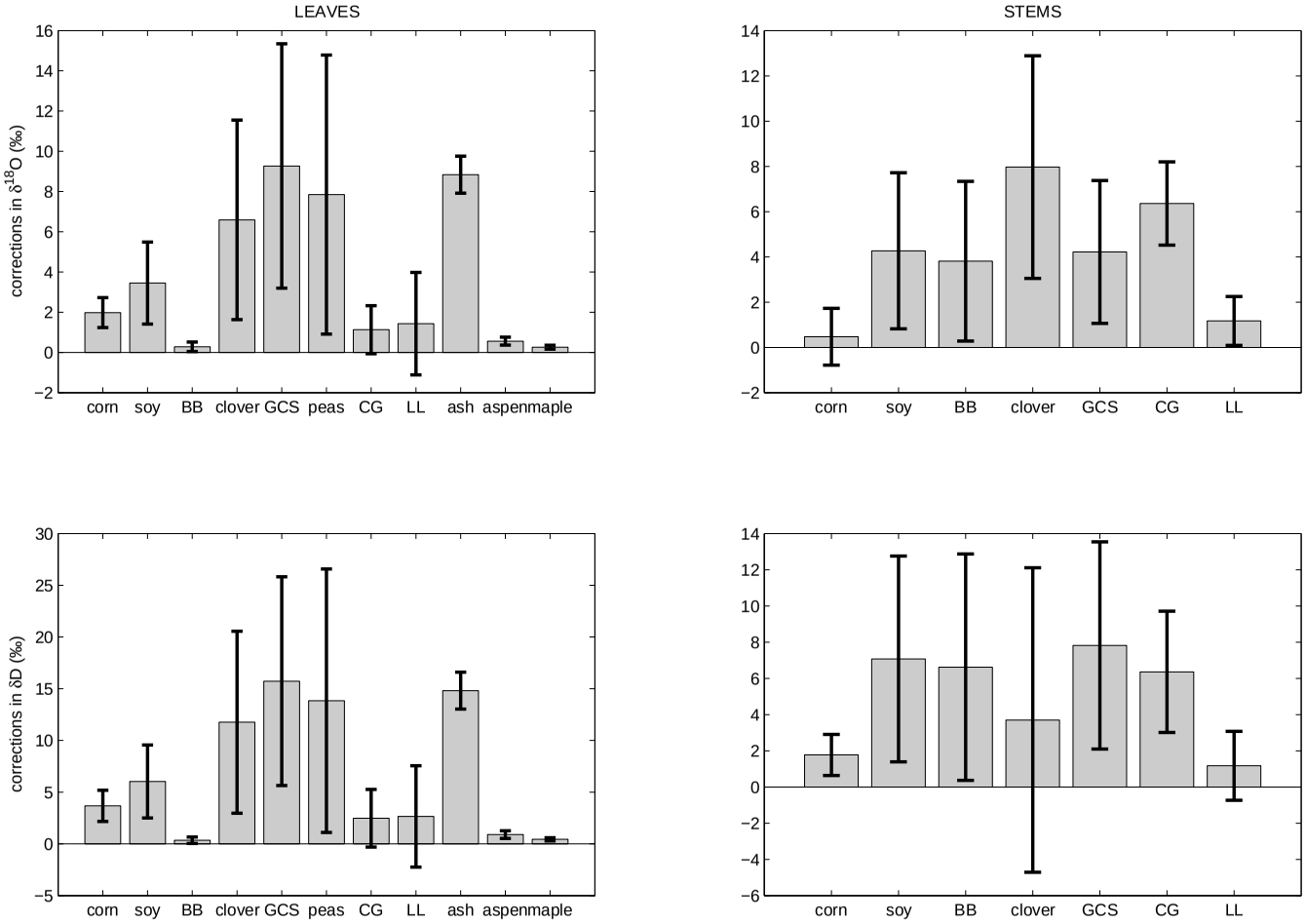

Figure 2.4: The corrected IRIS values of 78 leaf samples were compared to the same samples analyzed using IRMS in a double-blind comparison. Overall, the corrections eliminated the discrepancies between IRMS and IRIS for δ^{18}O, and greatly reduced the discrepancies for δ^{2}H. The mean differences in isotope ratios between IRMS and corrected IRIS methods was 0.19‰ for δ^{18}O, and -3.54‰ for δ^{2}H. The inability to create an ethanol correction curve for δ^{2}H likely caused the larger differences.

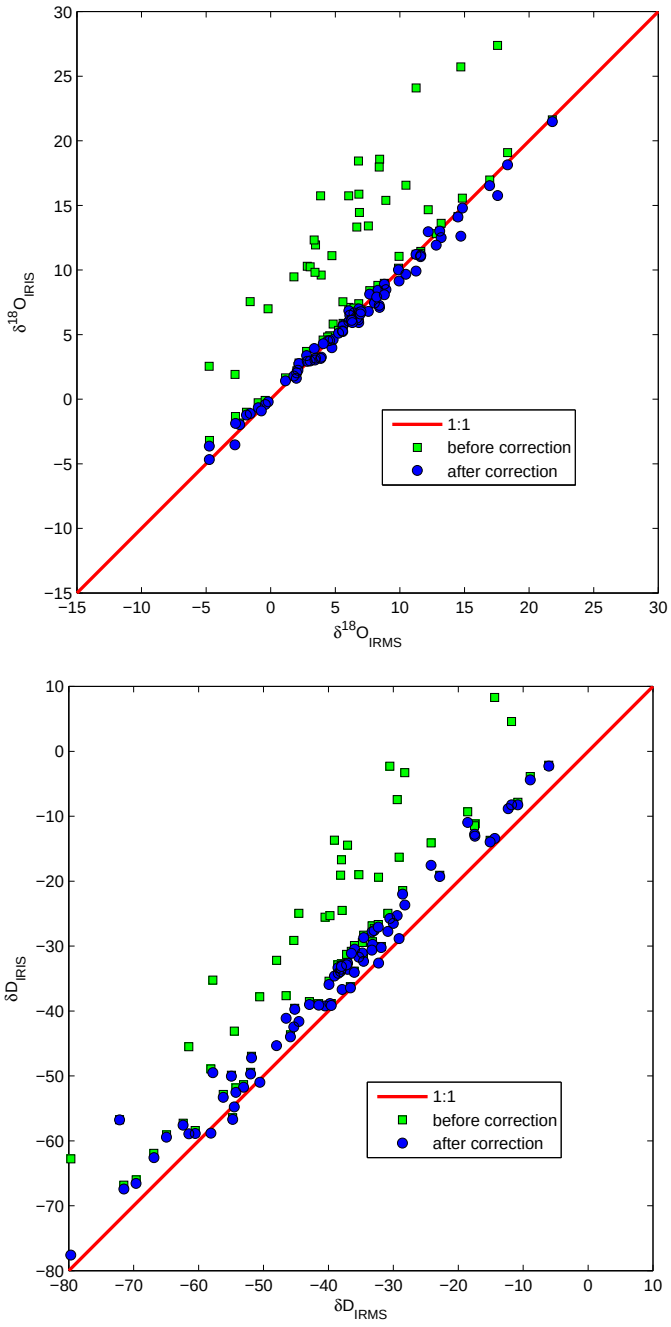

Chapter 3

Temporal variations in the isotope composition of water vapor and evapotranspiration observed from a tall tower within an agricultural landscape

Chapter Summary

Atmospheric water vapor has been increasing globally and over the central United States. The stable isotopes of water vapor can be used to better understand the processes controlling these trends, and help diagnose future change. The objectives of this research were to characterize the temporal variations in δ^{18}O, δ^{2}H, and *d*, and to investigate the mechanisms that influence the isotope ratios of water vapor at the landscape-scale in the atmospheric boundary layer. Here, δ^{18}O, δ^{2}H, and *d* in water vapor were continuously measured at 3m and 185m on a tall tower in Rosemount, MN, USA from May 2, 2010 through June 30, 2011. The isotopic forcing from evapotranspiration was also calculated. Large seasonal variations were observed in δ^{18}O, δ^{2}H, and *d*, with *d* in opposite phase with δ^{18}O and δ^{2}H. A distinct diurnal pattern was observed in δ^{18}O, δ^{2}H, and *d* that was especially prominent in the summer, with δ^{18}O and δ^{2}H being depleted during mid-day, and *d* enriched. The surface isoforcing was positive during mid-day hours for δ^{18}O and δ^{2}H, suggesting that entrainment dominated the diurnal signal of δ^{18}O and δ^{2}H. On average, δ^{18}O and δ^{2}H were more enriched near the surface. The largest vertical gradients were observed in the fall (September-November) and spring (March-May) seasons when evaporation from bare soil and open water bodies was more important. The *d* was more positive at 185m compared to 3m, potentially due to entrainment or partial evaporation of fog or raindrops.

3.1 Introduction

Atmospheric water vapor has been increasing over the past decades globally and over the central United States (McCarthy et al., 2009; Dai, 2006; Trenberth et al., 2005). These positive humidity trends are expected to be driven by surface warming, but changes in land use, atmospheric circulation and human water use may also be contributing factors. There is some evidence that anthropogenic influences are responsible for increases in specific humidity (Santer et al., 2007). The implications of increased water vapor are likely to be significant, but are still uncertain because of the complex role of water vapor in the climate system and the spatial variability of water vapor trends due to different feedbacks and forcing factors. Water vapor is the dominant greenhouse gas in the atmosphere, accounting for approximately 60% of the greenhouse effect (Keihl and Trenberth, 1997). The positive feedback resulting from increased atmospheric water vapor may intensify surface warming, affecting evaporation rates and precipitation intensity and or variability (Trenberth, 2011).

Changes in Minnesota's precipitation patterns are already evident. Positive precipitation trends have been observed over this region, with the Minnesota state-averaged precipitation reaching a maximum level of 889 mm in 2010, a 26% increase since the first recorded measurements in 1890 (www.climate.umn.edu). Precipitation normals at Waseca, MN have increased 30% since the 1921-1950 period from 700 mm to 910 mm (Seeley, 2010). Other characteristics of precipitation including intensity, frequency, and duration are expected to change with climate change (Trenberth, 2011; IPCC, 2007). A better understanding of the processes that control the transport of atmospheric moisture

are important in order to (1) anticipate future changes in the atmospheric water cycle and subsequent ecosystem responses and to (2) prepare societal adaptation strategies.

The stable isotopes of hydrogen and oxygen in water can be used as tracers to better understand the origin and the physical and biological processes involved in the transport of water throughout the atmosphere and biosphere (Gat, 1996). The isotope composition of water vapor is related to the source of moisture, and the complex processes such as surface evaporation, atmospheric mixing and transport, moisture recycling, and cloud formation that occur throughout the life cycle of an air mass (Angert et al., 2008; Lee et al., 2005). Because the biophysical processes involved in the land-atmosphere cycling of water uniquely alter the isotope ratios of hydrogen ($^{2}H/^{1}H$) and oxygen ($^{18}O/^{16}O$) in water, the isotope ratios can be used as tracers and diagnostics of environmental change.

It is useful to examine and quantify the modern relationships between meteorological variables and the isotope composition of precipitation and water vapor to accurately interpret long-term isotope records collected from climate proxies (e.g. ice cores, tree ring cellulose), and to inform isotopic parameters used in climate models (Vachon et al., 2010; Cuntz et al., 2003; Bowen and Wilkinson, 2002). In the past, researchers have used the modern empirical relationships between isotope ratios and climatological parameters (e.g. humidity, temperature, precipitation) to reconstruct historical climate change (e.g. (Petit et al., 1999; Wright and Leavitt, 2006)). A better understanding of how these relationships vary spatially and temporally will allow a more thorough analysis of past changes in climate and the use of isotope parameters in climate models.

The isotope ratios of precipitation have been widely studied and well documented. The

most prominent source for isotope variability in precipitation is the International Atomic Energy Agency's Global Network of Isotopes in Precipitation (IAEA-GNIP) (http://www-naweb.iaea.org/napc/ih/ IHS_resources_gnip.html). An early review of GNIP data by Dansgaard (1964) resulted in empirical relationships between isotope ratios of precipitation and the characteristics of the sampling site (e.g. latitude, altitude, continentality, precipitation amount, and surface air temperature). A comprehensive analysis of GNIP data performed by Rozanski et al. (1993) confirmed many of these early findings.

In the past, flask-sampling of water vapor was used for the collection of water vapor for isotope analysis (Angert et al., 2008; He and Smith, 1999; Jacob and Sonntag, 1991). Others have shown that over long (climatological) time scales, the isotope ratios of precipitation can be used to estimate the isotope composition of vapor in humid environments where direct measurements are not possible (Wen et al., 2010; Lee et al., 2006; Jacob and Sonntag, 1991). The disadvantage with this method, however, is that the measurements represent only a narrow set of meteorological conditions, and have shown to be very inaccurate for individual precipitation events (Wen et al., 2010; Lee et al., 2006; Jacob and Sonntag, 1991).

Recent technological advances have been made that allow continuous measurement of isotopes in the vapor phase (Griffis et al., 2010b; Iannone et al., 2010; Gupta et al., 2009; Lee et al., 2005). These new laser-based technologies have advanced to the point where they can be implemented in the field for long-term measurements. Continuous measurements of water vapor isotopes have the advantages of recording isotope variations over a range of temporal scales and under diverse environmental conditions. Optical water vapor

isotope measurements are on the verge of being implemented on a large-scale. For instance, the new observatory network, National Ecological Observatory Network (NEON) (www.neoninc.org), will utilize stable isotope measurements to study atmospheric and hydrological processes, and to detect and forecast environmental changes across continental scales. Further, satellite observations of the isotope ratios of atmospheric water vapor have been useful in investigating moisture recycling processes and changes in the hydrological cycle on a global scale (Worden et al., 2007).

To date, there are still very limited water vapor isotope data. Some of the first campaigns to continuously measure δ^{18}O and δ^{2}H in the vapor phase have found considerable short-term variations in δ^{18}O and δ^{2}H in water vapor (Wen et al., 2010; Lee et al., 2006), underscoring the need for high-frequency measurements, and presenting the opportunity to resolve variations in the atmospheric water cycle over a range of temporal scales. Other studies have incorporated the variations of δ^{18}O in water vapor to help interpret the ^{18}O-CO_2 signal because the variations in δ^{18}O in atmospheric water vapor play a key role with respect to leaf water enrichment and ^{18}O-CO_2 discrimination (Griffis et al., 2011; Welp et al., 2008).

Previous measurements of δ^{18}O and δ^{2}H in the vapor phase have been limited to surface measurements in urban environments and forests (Wen et al., 2010; Lee et al., 2006), and short-term summer campaigns at the field-scale (Griffis et al., 2010b; Welp et al., 2008). Here, we gain insight into the mechanisms that control the isotope composition of water vapor at the landscape-scale by measuring δ^{18}O, δ^{2}H, and *d* in water vapor on a tall tower. This study represents the first long-term ($>$ 1 year) measurements of δ^{18}O

and δ^2H over the Midwest, United States, a region characterized by intensive agriculture and extreme climate variability.

Variations in δ^{18}O, δ^2H, and *d* in water vapor over this region may result from the rainout effects of distant moisture sources, amplified by pronounced seasonal temperature variations, and the seasonal changes in evapotranspiration (F_{ET}). Figure 3.1 presents a schematic of the major processes that influence the isotope composition of water vapor at this site (typical of a mid-continental site), as well as the average values of δ^{18}O and δ^2H in water vapor, precipitation, and surface water pools (lakes, rivers, plant, soil, and groundwater).

In this study, we make use of the well-defined parameters, the Global Meteoric Water Line (GMWL) (Craig, 1961), and deuterium-excess (*d*) (Dansgaard, 1964), to aid in our interpretation of the biophysical mechanisms that are important in the local and large-scale transport of water, and to serve as a benchmark for understanding future hydrological changes that may caused by climate change or land use change. The *d* parameter is an important diagnostic that provides useful information about the evaporative source region and evaporative effects along an air mass trajectory that cannot be obtained from δ^{18}O or δ^2H individually. The *d* is a useful tool because it is conserved in an air mass unless kinetic fractionation effects related to evaporation occur. Here, *d* provides information about the causes of water vapor isotope variability that cannot be obtained from δ^{18}O or δ^2H alone.

In order to fully utilize the tracer capacity of the isotope ratios of water vapor, precipitation, and surface water sources, and the potential of these species to help forecast

future change, we must first understand how these species relate to the current meteorological and climatological conditions. By conducting a comprehensive analysis of water vapor, precipitation, and surface water sources, we can gain insight into the physical and biological processes that are important in the local and large-scale transport of water and help diagnose environmental and hydrological change. The objectives of this paper are therefore to characterize the temporal variations in δ^{18}O, δ^{2}H, and *d* in water vapor in the atmospheric boundary layer (ABL), and to investigate the mechanisms that influence these variations on annual, seasonal, and diurnal time scales. The main questions we seek to answer with this study are:

(1) What are the dominant mechanisms at the landscape-scale that influence δ^{18}O, δ^{2}H and *d* in the ABL in Rosemount, MN, USA?

(2) How are the temporal variations in δ^{18}O, δ^{2}H and *d* related to local meteorology?

(3) How do δ^{18}O, δ^{2}H and *d* vary vertically in the ABL? What mechanisms are responsible for these gradients?

(4) How do local sources of moisture (plant transpiration, evaporation from bare soil and water bodies) influence δ^{18}O, δ^{2}H and *d* in atmospheric water vapor?

3.2 Methods

3.2.1 Research Site Characteristics

Measurements of δ^{18}O and δ^{2}H in atmospheric water vapor were made at the Trace Gas Observatory (TGO) (Griffis et al., 2010a) at the Rosemount Research and Outreach

Center at the University of Minnesota (45° N, 93° W) from May 2 (DOY 122), 2010 through June 30 (DOY 181), 2011. The TGO (Minnesota Public Radio communications tower), is situated near the center of Dakota County, MN, where nearly 55% of the land is used for agriculture, 23% is low to medium-density suburban developments, with the remaining 22% of the land cover consisting of forests, grasses and shrubs, wetlands, and open water. The dominant agricultural crops are corn (*Zea mays L.*) and soybean (*Glycine Max*). Local land classification maps show that approximately 75% of land within a 5 km radius of the TGO is used for agriculture (30.1% corn, 21.4% soybean, 23% other) with smaller areas within this radius consisting of shrub/grasslands, broadleaf and conifer trees, and wetlands (Griffis et al., 2010a).

Minnesota climate is characterized by large seasonal variations in temperature and precipitation. During the summer months, warm moist air from the Gulf of Mexico and the southern United States advects into Minnesota. In the winter, the weather patterns are dominated by continental polar air with occasional Arctic outbreaks. Air masses from the Pacific Ocean move through Minnesota throughout the entire year, bringing mild and dry weather (NCDC, 2004a). The average annual temperature in Rosemount, MN is 6.4°C, with the average minimum monthly temperature in January of -12.2°C and an average maximum monthly temperature in July of 21.7°C. Annual temperature extremes range from -38.9°C to 40.6°C. The average annual precipitation in Rosemount, MN is 879 millimeters, with the greatest average monthly precipitation totals occurring from May through September (NCDC, 2004b).

3.2.2 Measurements of δ^{18}O and δ^{2}H in Water Vapor and Calibration Techniques

The water vapor measurements of δ^{18}O and δ^{2}H were conducted using a lead-salt tunable diode laser (TDL) (TGA200, Campbell Scientific Inc., Logan, Utah, USA). The technical specifications, a schematic diagram, and the air sampling and calibration procedures of the tunable diode laser (TDL) sampling system are given in detail by Griffis et al. (2010b). In this experiment, ambient air was drawn into the TDL from two inlets on the TGO mounted approximately 3 meters and 185 meters above the surface via Synflex tubing. Recently, Sturm and Knohl (2010) reported that Synflex had a slower equilibration time and potential kinetic fractionation effects on deuterium. Laboratory tests by Griffis et al. (2010b) confirmed the longer equilibration time when compared to HDPE (high density polyethylene) and Teflon, but did not confirm a kinetic fractionation effect for deuterium. Further, Lee et al. (2005) have used long sample lines of about 50 meters in length without observing adverse isotope effects.

The calibration procedure consisted of ultra dry air produced using compressed air passed through a nafion dryer and two molecular sieves mixed with water vapor generated from a dripper system that was capable of producing three different water vapor span values with an identical isotope composition. It was shown by Lee et al. (2005) and Griffis et al. (2010b) that the TDL sensitivity to water vapor mixing ratio was strongly non-linear. Griffis et al. (2010b) found the sensitivity of δ^{18}O to a change in mixing ratio to be approximately $1‰$ per mmol mol^{-1}. Because of this non-linear response, and the large temporal variations and vertical gradient in water vapor mixing ratio at the TGO,

a dynamic calibration technique was used to span the ambient water vapor mixing ratios of each inlet to within approximately 10%. Figure 3.2 shows an example of the dynamic calibrations over the period DOY 165 - DOY 166, 2011.

The sampling scheme consisted of a 10-min (600s) cycle: (1) calibration with dry air (110s), (2) calibration with the three span values (15s/each) for the 3m inlet, (3) sampling of the 3m inlet (145s), (4) dry air calibration, (5) calibration with the three span values (15s/each) for the 185m inlet, and (6) sampling of the 185m inlet (145s). An omit time of 5s was used on the calibration spans and air samples , and a 50s omit time was used for the dry air calibration. All raw data were recorded at 10 Hz using a datalogger and then averaged into one hour intervals. Further details on post-processing calibration techniques are described by Griffis et al. (2010b). Meteorological variables (i.e. relative humidity, temperature, precipitation) were measured and recorded at half-hour intervals throughout the sampling period. The independently measured relative humidity was used to screen out any periods of line condensation.

The measurement precision of a previous version of the TDL was reported by Wen et al. (2008). At a mixing ratio of 15.9 mmol mol^{-1}, the 25 second and one hour precision for δ^{18}O was 0.33‰ and 0.07‰, respectively, and 3.2‰ and 1.1‰ for δ^{2}H at the same mixing ratio. They showed that the precision of the instrument worsened slightly at lower mixing ratios. At 5.6 mmol mol^{-1} the 25 second and 1 hour precision was 0.66‰ and 0.12‰ for δ^{18}O and 11.3‰ and 2.0‰ for δ^{2}H.

3.2.3 Water Vapor Flux Measurements

The total water vapor flux (F_{ET}) at the TGO was derived from the field-scale water vapor flux measurements over corn and soybean canopies in 2010. Each water vapor flux at the individual field scale was determined via eddy covariance (EC) using a sonic anemometer (CSAT3, Campbell Scientific Incorporated) and an infrared gas analyzer (IRGA, LI-7500, Licor, Incorporated, Lincoln Nebraska, United States) mounted approximately 3m above the top of the canopies (Baker and Griffis, 2005). The total water vapor flux at the TGO was calculated to be a mean of these two fluxes. These measurements were found to be representative of the water vapor flux within the TGO footprint (approximately 5km) by comparing a previous year (2008) when water vapor fluxes were also being measured at the TGO using EC.

The isotope ratio of the water vapor flux (Griffis et al., 2004) was calculated hourly according to Eq 3.1.

$$F^i/F = \frac{X_2^i - X_1^i}{X_2 - X_1} \tag{3.1}$$

where F^i/F is the isotope ratio of the water vapor flux, F^i representing the heavy isotopologue ($H_2^{18}O$ or $^2H^1H_{16}O$), and X is the molar mixing ratio of the heavy or light isotopologue at 3m (X_1) or 185m (X_2). The flux ratio was then converted to delta (δ) notation relative to VSMOW:

$$\delta_{ET} = (\frac{F^i/F}{R_{VSMOW}} - 1) \times 1000. \tag{3.2}$$

Lastly, in order to quantify the local land cover influence on the isotope composition

of water vapor in the ABL, the isotopic forcing (I_F) was calculated for both hydrogen and oxygen isotopes (Lee et al., 2009):

$$I_F = \frac{F_{ET}}{C_a}(\delta_{ET} - \delta_a) \tag{3.3}$$

where C_a is the molar concentration of water vapor (in mmol m^{-3}) and δ_a is the isotope ratio ($\delta^{18}O$ or $\delta^{2}H$) of atmospheric water vapor.

3.2.4 Liquid Water Sampling and Isotope Analysis

Precipitation samples were collected from the University of Minnesota Rosemount Research and Outreach Center (RROC), and at the University of Minnesota-Saint Paul campus from January, 2006 through June, 2011 using a typical all-weather rain gauge with mineral oil added to eliminate evaporative fractionation effects. A total of 200 precipitation events have been collected and analyzed for their isotope ratios. During the course of the nearly six years of precipitation collection, sampling time varied from immediately after a precipitation event to a week after precipitation. Some samples contain more than one precipitation event. Snow samples were collected immediately following snow events. All samples were transferred to vials, sealed with Parafilm (a self sealing agent), and refrigerated until analysis. Rainfall time and amount was recorded using a tipping bucket rain gauge, and snowfall was measured using a snowboard.

Leaf, stem, and soil samples were collected from within a 5 km radius of the TGO during the growing season in 2011. Vegetation sampling sites chosen for this analysis were representative of the local land cover characteristics. A total of three soybean sites, three

corn sites, and three grass sites were sampled weekly between DOY 147 and DOY 243, 2010. The sampling protocol given by the Moisture Isotopes in the Biosphere and Atmosphere (MIBA) program (http://www-naweb.iaea.org/napc/ih/IHS_resources_miba.html) was followed. Briefly, sunlit leaves, non-green stems, and soil approximately 10cm below the surface were collected near midday (12:00 local standard time (LST)). Cryogenic vacuum distillation (West et al., 2006) was used to extract water from the plant and soil samples. Surface (i.e. lake & river) water and ground water samples were also collected from an approximately 25 km radius of the TGO.

All liquid water samples were analyzed for their isotope composition using a laser spectroscopy system (Liquid Water Isotope Analyzer, DLT-100, Los Gatos Research, Inc., Mountain View, California) coupled to an autosampler (HT-300A, HTA s.r.l., Brescia, Italy) for simultaneous measurements of ^{2}H/^{1}H and ^{18}O/^{16}O. This instrument has a precision of $\pm$1.0‰ for δ^{2}H and $\pm$0.25‰ for δ^{18}O. Pre-calibrated internal laboratory standards used to calibrate the unknown samples to VSMOW were selected based on the expected isotope composition of the unknown samples, and were injected after every two unknown samples to correct for instrumental drift. Linear calibration equations were calculated using each set of standards throughout the autorun and used to correct unknown samples. Sample quality was ensured by maintaining the operating equipment (i.e. frequent septum changes to avoid leakage, syringe washing to reduce salt precipitate buildup) to produce consistent injection volumes.

Recently, it has been shown that water extracted from plant and soil samples may contain organic materials that may interfere with the spectral signal from isotope ratio

infrared spectroscopy methods, resulting in erroneous isotope values (e.g. West et al., 2010; Brand et al., 2009; Zhao et al., 2011). Schultz et al. (2011) showed that it is possible to correct for spectral interference by spiking deionized water with the suspected contaminants, observing the degree of spectral interference with post-processing software, thus creating correction curves for unknown sample contamination. This correction method eliminated the discrepancies between spectroscopy and mass spectrometry methods in δ^{18}O, and greatly reduced the discrepancies in δ^{2}H. This correction methodology was employed here with the leaf and stem samples collected near the TGO. There were no instances of contamination in the soil samples. Following the findings of Schultz et al. (2011), the precision of the leaf and stem measurements is estimated to be 2.0‰ for δ^{2}H, and 0.58‰ for δ^{18}O.

3.3 Results & Discussion

3.3.1 Temporal Variations

Seasonal Variations

Figure 3.3 presents a time series of hourly δ^{18}O, δ^{2}H, and *d* in atmospheric water vapor observed at 3m and 185m from May 2 (DOY 122), 2010 through June 30 (DOY 181), 2011. To our best knowledge, this time series is the first of its kind over an agricultural landscape, and the first measurements of δ^{18}O, δ^{2}H, and *d* in water vapor in the mixed layer. Also shown are the event-based δ^{18}O, δ^{2}H, and *d* of precipitation during this same time period. Table 3.1 summarizes the monthly mean values of δ^{18}O, δ^{2}H, and *d* in water

vapor and precipitation. The monthly mean values of δ^{18}O, δ^{2}H, and *d* in precipitation are weighted by precipitation amount.

Over the entire time series, the average δ^{18}O, δ^{2}H, and *d* values were -27.2‰, -185‰, and 31.7‰ at 3m, and -28.3‰, -189.7‰, and 36.8‰ at 185m. There were large seasonal variations in the isotope ratios of water vapor. During the summer months, δ^{18}O and δ^{2}H in water vapor were highly enriched compared to winter months. The summer (JJA) averages of δ^{18}O and δ^{2}H were -17.7‰ and -123.3‰ at 3m, and -19.2‰ and -129.9‰ at 185m. The winter (DJF) averages of δ^{18}O and δ^{2}H were -37.3‰ and -241.2‰ at 3m, and -41.6‰ and -263.4‰ at 185m. The *d* in water vapor was in opposite phase with δ^{18}O and δ^{2}H. During the summer, the average *d* was 18.3‰ and 23.7‰ at 3m and 185m, respectively. In the winter, the average *d* at 3m and 185m was 48.6‰ and 50.0‰. The higher *d* in winter months is likely caused by stronger kinetic effects involved in the phase change from vapor to ice (Jouzel, 2007).

Our seasonal patterns agree with the general pattern in δ^{18}O in vapor observed in New Haven, CT, USA (Lee et al., 2006), where the highest monthly mean value of δ^{18}O occurred in May (-15.1‰), and the lowest monthly mean occurred in January (-29.4‰). We observed similar values of δ^{18}O in the summer months, but our δ^{18}O was more depleted by approximately 12‰ in the winter months compared to the New Haven measurements. New Haven is situated near a large water body (Long Island Sound, adjacent to the Atlantic Ocean), which moderates seasonal fluctuations in temperature. During the winter months, the temperature at our site was approximately 9°C colder than in New Haven, which likely caused larger isotope fractionation effects, and lower values of δ^{18}O and δ^{2}H

in water vapor. Our winter measurements of δ^{18}O and δ^{2}H were also more depleted than measurements in Beijing, China, by approximately 11‰ and 46‰ (Wen et al., 2010), but similar during summer months. Our monthly mean values of *d* were significantly higher than those observed in Beijing, where the maximum *d* observed in vapor ranged from 5.7‰ to 19.6‰. The *d* in vapor was lower, and significantly less variable in Beijing during the summer months (JJA) during peak monsoon activity (Wen et al., 2010). In contrast, more frequent frontal activities in addition to seasonal evaporative effects likely contributed to the larger intra-seasonal variability in *d* during summer months at our site.

The seasonal variations in δ^{18}O and δ^{2}H were correlated with the water vapor mixing ratio (*w*). The relationships between *w* and δ^{18}O and δ^{2}H were log-linear. At 3m, the relationships between *w* and δ^{18}O and δ^{2}H were $\delta^{18}O = 9.8 \times \ln w - 47.0$ ($R^2 = 0.76$) and $\delta^{2}H = 65.4 \times \ln w - 318.8$ ($R^2 = 0.68$). At 185m, the correlations were similar: $\delta^{18}O = 9.7 \times \ln w - 47.3$ ($R^2 = 0.73$) and $\delta^{2}H = 63.8 \times \ln w - 316.8$ ($R^2 = 0.65$). The dependence of δ^{18}O and δ^{2}H on the water vapor mixing ratio indicate that Rayleigh distillation was the dominant mechanism explaining the seasonal variations in the isotope composition of water vapor.

On shorter timescales, δ^{18}O, δ^{2}H, and *d* in water vapor could vary day-to-day by more than 25‰, 175‰, and 75‰, respectively, due to changing meteorological conditions. For instance, in the days leading up to DOY 226, 2010, warm, moist air was in place over the region, with heat advisories in effect for several days. A cold front moved through the region on DOY 226, bringing in cooler and drier air. The isotope ratios of water vapor changed dramatically as this weather system moved through, with before and after

differences as large as 20‰, 175‰, and 75‰ for δ^{18}O, δ^{2}H, and *d*, respectively.

The seasonal variations in δ^{18}O and δ^{2}H in vapor were positively correlated with δ^{18}O and δ^{2}H in precipitation. In general, δ^{18}O and δ^{2}H in precipitation were higher in the warm months than in the cold months. On average, the δ^{18}O and δ^{2}H values of precipitation were enriched 18.0‰ and 124.2‰, respectively, compared to water vapor. The highest monthly mean values of δ^{18}O and δ^{2}H in precipitation of -4.57‰ and -25.61‰ were observed in August, 2010. The lowest monthly mean values of -23.67‰ and -186.21‰ were observed in January, 2011. The seasonal pattern in δ^{18}O and δ^{2}H in precipitation follows the seasonal pattern observed in previous years (Figure 3.4), and the seasonal pattern in precipitation at other mid-latitude sites from the GNIP network (Rozanski et al., 1993). The *d* in precipitation was significantly lower than *d* in water vapor during the warm seasons, likely indicating partial raindrop evaporation, a process that decreases the *d* of precipitation, and increases the *d* of vapor (Jacob and Sonntag, 1991). The monthly mean of *d* in precipitation reached its highest value (20.36‰) in November, 2010, and lowest value (3.16‰) in March, 2011. Notably high *d* values were also observed in water vapor in November (55.7‰ at 3m, and 62.0‰ at 185m). During November, evaporation from bare soils and open water bodies may have been contributing factors in the high *d* values. Back-trajectory analysis using HYSPLIT (not shown here) (Draxler and Rolph, 2010) and analysis of wind-direction during November showed that northerly flow dominated during this time period, potentially including evaporation from Lake Superior. The low *d* in precipitation in January, 2011, was not associated with particularly low *d* values in water vapor.

Diurnal Variations

Figure 3.5 presents the 24 hour ensemble average values of δ^{18}O, δ^{2}H, and *d* in water vapor at 3m and 185m. The full time series is broken up into four seasons: spring (March-May), summer (June-August), fall (September-November), and winter (December-February). Also shown are the diurnal cycles for the water vapor mixing ratio (*w*) and relative humidity (*h*).

During the spring, summer, and fall seasons, δ^{18}O and δ^{2}H were relatively depleted at 185m compared to 3m during most hours; however, during mid-day, there was little to no difference in δ^{18}O and δ^{2}H at the different inlet heights. This is evidence of a well mixed boundary layer caused by surface heating and convective turbulence. As the surface cools during the evening and overnight hours, the stabilization of the atmosphere causes air stratification and the strong vertical gradient of δ^{18}O and δ^{2}H. The diurnal *d* pattern was not in phase with the diurnal patterns of δ^{18}O and δ^{2}H. The *d* was relatively enriched at 185m, *d* peaked during mid-day and reached a minimum near midnight. During the winter, there was little difference in δ^{18}O, δ^{2}H, and *d* over most hours of the day.

There was an obvious diurnal pattern in δ^{18}O and δ^{2}H in the summer that was more prominent at 3m. Both δ^{18}O and δ^{2}H were relatively depleted during mid-day, and enriched during the evening to early morning hours. Griffis et al. (2010b) showed positive isoforcing during mid-day hours in the summer when δ^{18}O was at its minimum. This mid-day decrease of δ^{18}O and δ^{2}H has been attributed to the entrainment of dry, isotopically depleted air from above the ABL (Lai and Ehleringer, 2011; Griffis et al., 2010b; Welp et al., 2008; Lee et al., 2006). In contrast, the values of δ^{18}O and δ^{2}H in winter showed a

different pattern, peaking during mid-day hours, and decreasing overnight. This pattern was especially prominent in δ^{18}O at 185m. The average values of δ^{18}O and δ^{2}H in snow during the winter season were -21.3‰ and -166.3‰, respectively. It may be possible that snow sublimation or snowmelt evaporation were factors in the mid-day winter enrichment of δ^{18}O and δ^{2}H. Lee et al. (2006) and Wen et al. (2010) observed similar diurnal patterns in the diurnal cycles of δ^{18}O and δ^{2}H across spring, summer, and fall seasons, despite different land cover characteristics (both urban sites). In contrast, they did not observe the mid-day peak during the winter. The diurnal variations in δ^{18}O and δ^{2}H appeared to be in phase with variations in *w*. The diurnal pattern of *d* was in opposite phase with δ^{18}O and δ^{2}H during the summer, peaking during mid-day and reaching a minimum near midnight.

In order to understand the influence of local land cover on the diurnal patterns of δ^{18}O, δ^{2}H, and *d* in vapor, the isotope ratios of F_{ET} and isotopic forcing (I_F) were calculated. Evapotranspiration (F_{ET}), divided into four seasons, is shown in Figure 3.6. The largest flux was observed during the growing season, with an average mid-day peak of approximately 6.5 mmol m^{-2} s^{-1}. During the spring and fall, the maximum mid-day fluxes were approximately 2.0 and 1.5 mmol m^{-2} s^{-1}, respectively. The winter F_{ET} was much smaller, with an average mid-day peak of only 0.5 mmol m^{-2} s^{-1}.

The diurnal patterns of the isotope composition of F_{ET} ($\delta^{18}O_{ET}$, $\delta^{2}H_{ET}$, and d_{ET}), determined from the flux ratio method (Eq. 3.1), are shown in Figure 3.7. Note that the winter season was excluded from the δ^{2}H (and thus *d*) plots because of low signal to noise. During the summer (JJA) months, the mid-day values of $\delta^{18}O_{ET}$, $\delta^{2}H_{ET}$, and

d_{ET} agreed very well with the average isotope ratios of xylem water (δ_x) (dashed lines also shown on Figure 3.7), implying that isotopic steady state is reached during peak transpiration rates (Welp et al., 2008), that the tall tower flux ratios are representative of the plant source water, and that plant transpiration is the dominant influence on the flux ratio.

Welp et al. (2008) showed how the δ^{18}O of transpiration (δ_T) deviated from the δ^{18}O of xylem water (δ_x) over the course of a day: δ_T was less than δ_x in the morning, but as the δ^{18}O of leaf water increased progressively during the day, δ_T became greater than δ_x in the late afternoon and evening. Theoretically, *d* of transpiration (d_T) should be greater than *d* of xylem water (d_x) during the morning, and less than d_x in the evening (Welp et al., 2011). This was true for d_{ET} observed at the TGO in the summer season. The d_{ET} averaged over the growing season was negative during overnight hours (-60‰), peaked during mid-morning hours (40‰), and gradually decreased over the course of the day. Again, during mid-day, d_{ET} agreed very well with d_x, indicating that steady state conditions were met, and that transpiration dominated the summer d_{ET} signal.

The pattern of d_{ET} was slightly different during the spring and fall seasons, when evaporation from bare soil and open water is a larger component of F_{ET}. During both seasons, d_{ET} was negative during the early morning hours (-5 to -20‰). The diurnal pattern of d_{ET} averaged across the fall season rapidly increased after the early morning minimum, reached its peak of 85‰ during mid-day following peak solar radiation, and gradually decreased into evening and overnight hours. The diurnal pattern of spring d_{ET} followed the fall d_{ET} pattern from evening to early morning hours, but did not have the

strong peak during mid-day. The d_{ET} patterns in fall and spring were negatively correlated with *h*, peaking during low *h*, and reaching a minimum during high *h* (Figure 3.5).

Figure 3.8 presents the diurnal variations in $I_F\delta^{18}O$ and $I_F\delta^2H$. The isotopic forcing related to F_{ET} was positive for $\delta^{18}O$ and δ^2H across all seasons, indicating that F_{ET} enriches the surface air in the heavy isotopes of hydrogen and oxygen. The isoforcing peaked during mid-day hours across most seasons, and there was a small but noticeable positive isoforcing during the winter.

We attempt to further explain the diurnal patterns in $\delta^{18}O$, δ^2H, and *d* by applying the change in surface isoforcing ΔI_F in the one-dimensional rate equation (Lee et al., 2011):

$$\frac{\partial \delta}{\partial t} = \frac{1}{h}(\Delta I_F) \tag{3.4}$$

where h is the height of the ABL, and the change in isoforcing (ΔI_F) is defined here as the change in I_F over the diurnal cycle.

During the summer months, there was a mid-day depletion of approximately 1.5‰ and 7‰ in $\delta^{18}O$ and δ^2H in water vapor. If we use an estimate of 1400 meters for the mid-day summer ABL height, ΔI_F of 0.08 and 0.5‰ m s^{-1} for $\delta^{18}O$ and δ^2H, we can theoretically derive the total mid-day enrichment of $\delta^{18}O$ and δ^2H caused by ET. Using these parameters, we estimated that ET should result in a mid-day enrichment of 1.4‰ and 9.0‰ in $\delta^{18}O$ and δ^2H, respectively. These simple calculations support previous research that entrainment of isotopically depleted air from above the ABL dominates the diurnal patterns of $\delta^{18}O$ and δ^2H.

3.3.2 Vertical Variations

Over the entire time series, δ^{18}O and δ^{2}H were relatively enriched at 3m on average by 1.2‰ and 4.5‰ compared to 185m. Interestingly, *d* was consistently higher at 185m compared to 3m throughout the spring, summer, and fall seasons, in contrast to Lai and Ehleringer (2011), who showed *d* to be independent of height in the surface layer. Over the entire dataset, *d* was relatively depleted at 3m by 5.1‰. This result was a surprising, as we expected a higher *d* near the surface due to the kinetic fractionation effects associated with evaporation. We hypothesize that top-down diffusion or re-evaporation of fog droplets or raindrops may be potential factors contributing to this pattern. Model results by Lai and Ehleringer (2011) suggest a low *d* aloft that entrains into the ABL, causing low *d* values during the morning hours, with a more positive *d* in the afternoon hours consistent with the influence of ET. Contrarily, profile measurements of δ^{18}O and δ^{2}H up to nearly 3000 meters by He and Smith (1999) showed markedly lighter values of δ^{18}O and δ^{2}H above the ABL, characterized by a higher *d*.

A simple Rayleigh model was used to try to better understand the vertical isotope gradients (Lee et al., 2006):

$$\delta_v = \delta_{v,o} + (\alpha - 1) \ln \frac{w}{w_o} \tag{3.5}$$

where δ_v is the isotope ratio of δ^{18}O or δ^{2}H in water vapor, $\delta_{v,o}$ is the isotope ratio of the source, α is the temperature dependent equilibrium fractionation factor (Majoube, 1971), and w and w_o are the water vapor mixing ratio, and the mixing ratio at the source. Here,

the isotope values and mixing ratios at 3m were used to predict the isotope ratios at 185m. Overall, this equation predicted δ^{18}O and δ^{2}H at 185m to within 0.4‰ and 1.3‰ of the observed mean values, respectively, over-predicting δ^{18}O, and under-predicting δ^{2}H. In contrast, this Rayleigh model predicted a *d* at 185m 0.4‰ lower than the *d* at 3m, in stark contrast to the higher *d* observed at 185m. This result supports our hypothesis that entrainment or the evaporation of raindrops or fog droplets may be potential causes of the high *d* at 185m.

The greatest monthly differences between δ^{18}O, δ^{2}H, and *d* at 3m and 185m ($\delta_{3m} - \delta_{185m}$) were 2.1‰, 9.2‰, and -7.3‰, observed in September, 2010. In general, the largest differences in δ^{18}O, δ^{2}H, and *d* between the two inlet heights were observed in the fall and spring seasons, when evaporation from bare soil and open water makes up a larger proportion of ET. At this point, more research needs to be conducted to determine whether evaporation is driving these patterns, or if other processes (i.e. fog/raindrop evaporation, entrainment) are more important. The smallest differences between in δ^{18}O and δ^{2}H between 3m and 185m were observed in the winter months, with average differences of <0.1‰, 2.4‰, and -1.4‰, for δ^{18}O, δ^{2}H, and *d*.

Across the entire dataset, variations in δ^{18}O and δ^{2}H at 3m and 185m were generally well correlated. The relationships between δ^{18}O and δ^{2}H at 3m and 185m were $\delta^{18}O_{185m} = 0.96 \times \delta^{18}O_{3m}$ - 2.8 ($r = 0.96$, $p<0.001$), and $\delta^{2}H_{185m} = 0.78 \times \delta^{2}H_{3m}$ - 44.5 ($r = 0.80$, $p<0.001$). In contrast, variations in *d* at 3m and 185m were not well correlated ($d_{185m} = 0.34 \times d_{3m} + 25.9$, $r = 0.32$, $p<0.001$). At this point, it is not clear why there is such poor correlation in *d* between the two inlets.

3.3.3 Water Vapor in Equilibrium with Precipitation

Equilibrium theory was used to understand the relationship between the isotope ratios of precipitation and water vapor. In a saturated environment, isotope equilibrium is expected ($R_v = R_L/\alpha$) where R_v is the absolute isotope ratio ($^{18}O/^{16}O$ or $^{2}H/^{1}H$) of water vapor, α is the equilibrium fractionation factor, and R_L is the isotope ratio of precipitation. The equilibrium assumption is valid under saturated conditions; however, during rain events, the atmosphere can still be relatively dry, and equilibrium conditions may not be satisfied. If the atmosphere is unsaturated, we are likely to observe kinetic fractionation associated with surface or raindrop evaporation. Worden et al. (2007) found that rainfall evaporation in the tropics contributed significantly to lower troposphere humidity. Here, we examine if the isotope composition of vapor can be estimated using the isotope ratios of precipitation, thus providing additional information about the relative influences of equilibrium and kinetic fractionation processes on the isotope ratios of water vapor and precipitation, and the contributing factors to humidity changes in the ABL.

The equilibrium values of $\delta^{18}O$ and $\delta^{2}H$ in water vapor were calculated from the isotope ratios of individual rain events and the surface air temperature averaged over the rain event. The equilibrium values of $\delta^{18}O$ and $\delta^{2}H$ in water vapor were then averaged over the precipitation event, weighted by the precipitation amount. The equilibrium *d* was calculated using the equilibrium values of $\delta^{18}O$ and $\delta^{2}H$. Figure 3.9 presents the measured values of $\delta^{18}O$, $\delta^{2}H$ and *d* ($\delta^{18}O_v$, $\delta^{2}H_v$, d_v) in water vapor at 3m and 185m in 2010 and 2011 against the predicted equilibrium values of $\delta^{18}O$, $\delta^{2}H$ and *d* ($\delta^{18}O_{v,e}$, $\delta^{2}H_{v,e}$, $d_{v,e}$). There is good agreement overall between the measured and predicted values, however,

the predicted vapor values were biased high on average by 1.9‰ for δ^{18}O, and 7.5‰ for δ^{2}H, consistent with the expected effects from kinetic fractionation.

The *d* of water vapor was poorly predicted using the equilibrium method. With the exception of two events, the equilibrium method predicted the *d* of water vapor to generally be between 0‰ and 20‰. Measurements showed that the *d* of water vapor during precipitation events actually varied between -20‰ to 60‰. These findings confirm that kinetic fractionation occurring during below-cloud raindrop evaporation or land surface evaporation are important influences on the isotope ratios of precipitation and evaporation.

We expect better agreement between the measured vapor values and the equilibrium predictions of water vapor values during saturated conditions, and bigger differences as relative humidity decreases. Theoretically, the influence of kinetic fractionation effects should cause the equilibrium predictions to be higher than the measured water vapor isotope ratios, and this difference should increase with decreasing RH (Wen et al., 2010). The relative humidity (RH) during individual precipitation events in this study varied between approximately 75% and 100%. Here, at high RH (>95%), there was consistently low error between the measured and predicted values of individual events; however, at lower humidities, there was no clear relationship between RH and how well δ^{18}O or δ^{2}H was predicted. The *d* was better predicted under near saturated conditions (>95% RH), and was not well predicted under unsaturated conditions. Again, there was no clear trend between RH and the differences between measured *d* and predicted *d*.

3.3.4 δ^{18}O - δ^{2}H Relationships

Figure 3.10 presents the relationships between δ^{18}O and δ^{2}H in all sample types (precipitation, water vapor, soil water, stem water, leaf water, and surface water). Also shown as a reference is the GMWL ($\delta^{2}H = 8\times\delta^{18}O + 10$). Table 3.2 summarizes these results. The local meteoric water line (LMWL), the relationship between the monthly amount-weighted averages of δ^{18}O and δ^{2}H, is $\delta^{2}H = 8.0\times\delta^{18}O + 10.7$ ($R^2 = 0.98$). A LMWL at any geographic location may be quite different from the GMWL due to local meteorologic factors and fractionation processes (i.e. storm trajectories, local ET, and raindrop evaporation) (Peng et al., 2004). In our case, the long-term (6 year) LMWL agreed very well with the GMWL, indicating that on a time scale of years, local precipitation is derived from oceanic sources. The δ^{18}O - δ^{2}H regression of precipitation (not weighted by precipitation amount) varied slightly from the LWML, with a lower slope, intercept, and *d*, suggesting the influence of below-cloud evaporation during small precipitation events.

Water undergoing evaporation is characterized by a slope lower than 8 and a low *d* because of the stronger kinetic effects for ^{18}O relative to ^{2}H. Analysis of the relationships between δ^{18}O and δ^{2}H in local water pools may help us understand how the isotope composition of water vapor is influenced by local evaporation. Here, we observe slopes much lower than 8 in the δ^{18}O - δ^{2}H relationships in soil, stem, leaf, and surface water. The lowest slope (2.7) is observed in mid-day ($\approx$ 12:00 LST) leaf water (d = -52.5‰). Evaporating water from nearby lakes and rivers had a slope of 4.8 and a *d* of -4.5. Soil water sampled at a depth of 10 cm showed characteristics of evaporation (a slope of 5.3, and a *d* of -5.7). Interestingly, the water extracted from the stems of plants also showed

evaporation characteristics (slope = 5.8, d = -0.3), despite the uptake of water being a non-fractionating process. That these characteristics of stem water are similar to those of soil water may potentially indicate the uptake of water from roots at shallower soil depths.

The δ^{18}O - δ^{2}H relationships in water vapor were characterized by lower slopes (6.1 and 5.9 for 3m and 185m, respectively) and high d values (31.7‰ and 36.8‰). If water vapor were in equilibrium with precipitation, the δ^{18}O - δ^{2}H relationships in water vapor would follow the LWML. Indeed, calculations of water vapor in equilibrium with precipitation resulted in a slope and d close to the LMWL (slope = 7.0, d = 10.2‰). During warm season precipitation events, the δ^{18}O - δ^{2}H relationship in water vapor was δ^{2}H = 6.0×δ^{18}O - 20.8 (d = 18.0‰), while the δ^{18}O - δ^{2}H relationship of precipitation was δ^{2}H = 7.1×δ^{18}O +0.91 (d = 7.1). The relatively higher d in vapor during precipitation events likely indicates the influences of ET and below-cloud raindrop evaporation.

Overall, the characteristics of the relationships between δ^{18}O and δ^{2}H in vapor exhibit influences of surface and raindrop evaporation. Here, these relationships in water vapor provide additional information than could have been gathered from precipitation alone. Future research may focus on using δ^{18}O - δ^{2}H relationships to quantify the relative influences of evaporation and transpiration on the isotope composition of local water vapor. Analysis of both δ^{18}O and δ^{2}H in water vapor may provide early detection of changes in evaporation processes that may affect local atmospheric humidity.

3.4 Conclusions

In this paper, δ^{18}O, δ^{2}H, and *d* in water vapor were measured at 3m and 185m on a tall tower in Rosemount, MN from May 2, 2010 to June 30, 2011. The temporal and vertical variations in the isotope composition of water vapor were observed, and the meteorological mechanisms that influenced these variations were investigated. These data are the longest continuous measurements of the isotope composition of water vapor over an agricultural landscape, and are the first continuous measurements in the mixed layer. The main conclusions are as follows:

(1) On average, δ^{18}O and δ^{2}H were 1.2‰ and 4.1‰ enriched at 3m compared to 185m. Interestingly, *d* was depleted by, on average, 5.1‰ at 3m. We hypothesize that entrainment or the re-evaporation of fog or cloud droplets was responsible for the higher *d* at 185m. The smallest vertical gradients in δ^{18}O, δ^{2}H, and *d* were observed during mid-day hours due to turbulent mixing of the ABL. The largest vertical gradients were observed in the fall and spring seasons, when evaporation from bare soil and open water bodies was a larger component of F_{ET}. The smallest vertical gradients were observed in the winter.

(2) There was an obvious diurnal pattern in δ^{18}O, δ^{2}H, and *d* in the spring, summer, and fall seasons, that was especially prominent during the summer months. Both δ^{18}O and δ^{2}H were relatively depleted during mid-day. F_{ET} was shown to enrich the atmosphere in δ^{18}O and δ^{2}H by 1.4‰ and 9.0‰, respectively. The mid-day isotope depletion was likely caused by the entrainment of dry, isotopically depleted air from above the boundary layer.

(3) The isotope composition of F_{ET} ($\delta^{18}O_{ET}$, $\delta^{2}H_{ET}$, d_{ET}) was determined from TGO isotope gradients. During the summer months, the mid-day values of $\delta^{18}O_{ET}$, $\delta^{2}H_{ET}$, and d_{ET} agreed very well with the seasonal average of δ_x, suggesting that plant transpiration dominated the summer F_{ET} signal, and that isotopic steady state was reached during peak transpiration rates. The d_{ET} during summer was greatest during early morning hours, and gradually decreased throughout the course of a day. During the fall and spring seasons, the diurnal d_{ET} pattern was different, following the solar radiation pattern, and peaking during mid-day.

(4) The relationships between $\delta^{18}O$ and $\delta^{2}H$ in water vapor exhibited characteristics indicative of surface and raindrop evaporation influences. These relationships were characterized by low slopes and high *d* values. The LMWL closely agreed with the GMWL, however the $\delta^{18}O$ - $\delta^{2}H$ regression of individual precipitation events suggested the influence of below-cloud evaporation during small precipitation events. Water from soil, open water, and leaves had low slopes and low *d* values, characteristic of water undergoing evaporation.

In future work, we will further investigate this dataset in conjunction with satellite observations and atmospheric transport models (e.g. STILT) to try to quantify how changes in surface (i.e. evaporation, transpiration) and atmospheric (i.e. circulation patterns, entrainment) processes cause variations in $\delta^{18}O$, $\delta^{2}H$, and *d* of water vapor in the ABL. We hope to provide new information on the transport and recycling of water vapor in the atmosphere, and ultimately better understand how climate variations and local land cover change will alter the atmospheric water cycle.

Table 3.1: Monthly average values of temperature (T), relative humidity (RH), precipitation (P), water vapor mixing ratio (w) at 3m and 185m, and the isotope ratios of precipitation and water vapor at 3m and 185m. The water vapor mixing ratios are reported in mmol mol^{-1}, and all isotope ratios are reported in permil (‰)

				Precipitation			Vapor 3m				Vapor 185m			
Date	T (° C)	RH (%)	P (mm)	δ^2H	δ^{18}O	d	δ^2H	δ^{18}O	d	w	δ^2H	δ^{18}O	d	w
Jun-2010	19.4	81.2	169.3	-50.5	-7.8	11.8	-140.9	-20.2	20.7	19.6	-147.2	-21.9	27.7	18.7
Jul-2010	22.5	82.8	171.5	-58.3	-8.3	7.9	-121.4	-17.3	17.2	24.6	-129.7	-19.1	23.2	22.7
Aug-2010	22.3	85.8	153.8	-25.6	-4.6	10.9	-118.0	-17.1	19.0	23.5	-123.8	-18.5	24.0	22.4
Sep-2010	14.4	82.8	36.8	-57.9	-8.6	11.0	-166.4	-24.4	28.7	14.7	-175.6	-26.5	36.0	13.6
Oct-2010	10.4	72.4	39.5	-62.7	-9.9	16.3	-169.8	-25.1	30.7	9.4	-177.4	-26.7	36.3	8.9
Nov-2010	0.7	80.6	52.6	-43.5	-8.0	20.4	-209.1	-33.1	55.7	5.7	-212.1	-34.3	62.0	5.4
Dec-2010	-9.8	88.1	70.9	-153.0	-20.6	11.9	-265.0	-41.3	65.2	3.9	-262.7	-41.1	65.8	3.9
Jan-2011	-12.0	86.5	25.4	-186.2	-23.7	3.1	-280.7	-40.7	44.5	3.2	-284.2	-40.7	41.6	3.2
Feb-2011	-8.5	83.1	28.5	-81.2	-10.9	6.3	-248.9	-35.6	36.2	4.4	-243.4	-35.8	42.6	4.5
Mar-2011	-2.5	80.2	52.3	-58.3	-9.0	13.8	-193.9	-29.0	37.0	5.1	-201.2	-30.0	38.5	4.9
Apr-2011	6.7	75.2	70.5	-84.8	-11.6	7.7	-176.6	-24.6	20.4	7.6	-179.4	-25.8	26.4	7.1
May-2011	13.7	72.7	75.0	-32.5	-5.1	8.2	-142.3	-20.0	18.0	12.0	-150.6	-21.4	20.6	10.9
Jun-2011	19.5	77.5	31.3	-29.9	-5.3	12.4	-117.6	-16.6	15.4	17.9	-121.3	-17.5	18.5	16.7

Table 3.2: The relationships between δ^{18}O and δ^{2}H in precipitation, water vapor at 3m and 200m, soil water, stem water, leaf water, and surface (lakes and rivers) water, and the *d* for each water pool. n denotes the total number of samples, and *d* in reported in permil (‰).

sample type	n	δ^{18}O - δ^{2}H	R^2	*d*
precipitation	200	$\delta^{2}H = 7.8\times\delta^{18}O + 6.9$	0.97	8.4
vapor 3m	6746	$\delta^{2}H = 6.1\times\delta^{18}O$ - 21.3	0.79	31.7
vapor 185m	6746	$\delta^{2}H = 5.9\times\delta^{18}O$ - 22.9	0.75	36.8
soil	44	$\delta^{2}H = 5.3\times\delta^{18}O$ - 21.6	0.58	-5.7
stem	53	$\delta^{2}H = 5.8\times\delta^{18}O$ - 15.4	0.81	-0.3
leaf	87	$\delta^{2}H = 2.7\times\delta^{18}O$ - 37.1	0.44	-52.5
surface	32	$\delta^{2}H = 4.8\times\delta^{18}O$ - 18.9	0.96	-4.5

Figure 3.1: A schematic of the important processes that influence the isotope ratios of water vapor, and the average isotope composition of δ^{18}O and δ^{2}H in local water pools.

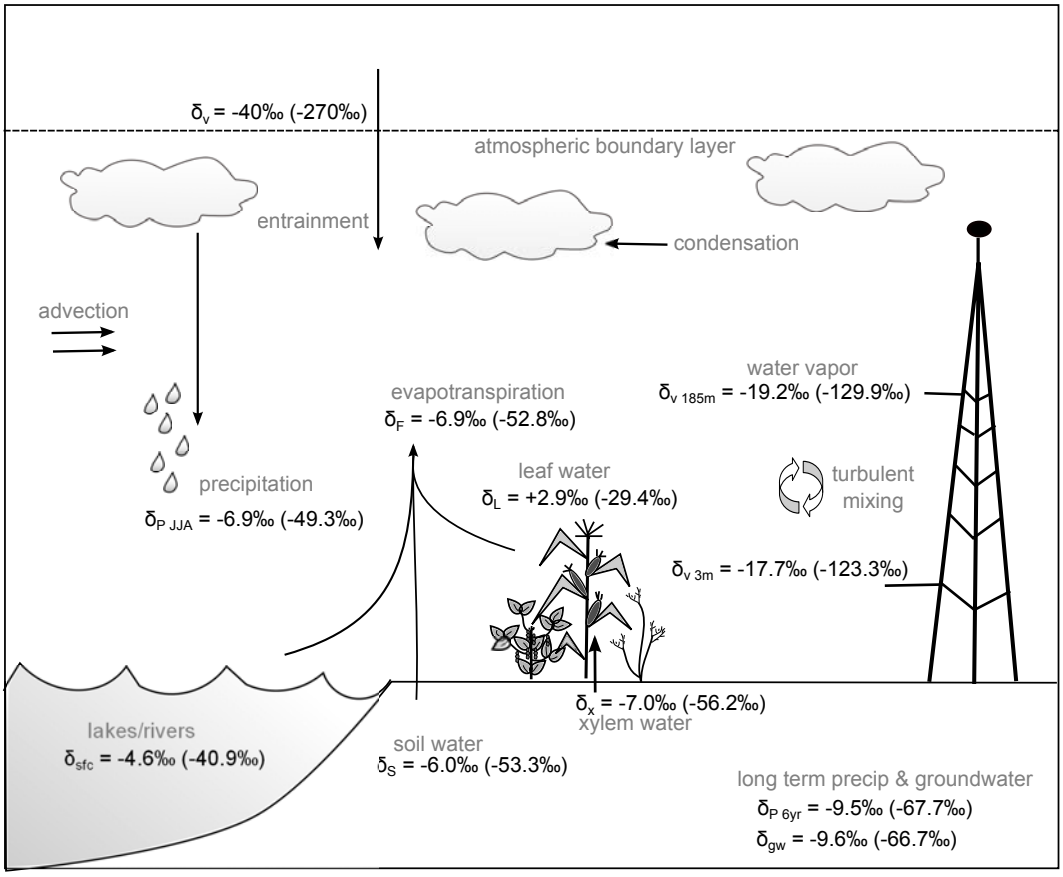

Figure 3.2: Example of the dynamic calibration used for δ^{18}O and δ^{2}H in water vapor at the tall tower from DOY 165 - DOY 166.

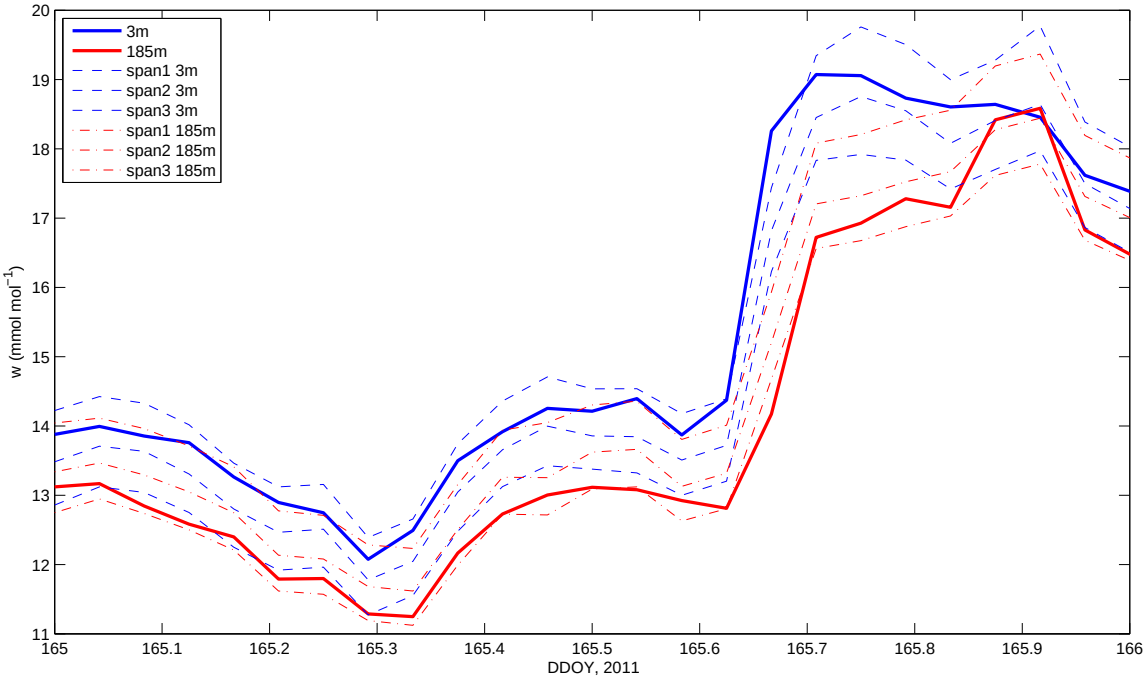

Figure 3.3: Time series of δ^{18}O, δ^{2}H, and d in water vapor and precipitation from May 2, 2010 through June 30, 2011. The blue and red dots represent hourly values of water vapor at 3m and 200m, and the triangles represent individual precipitation events.

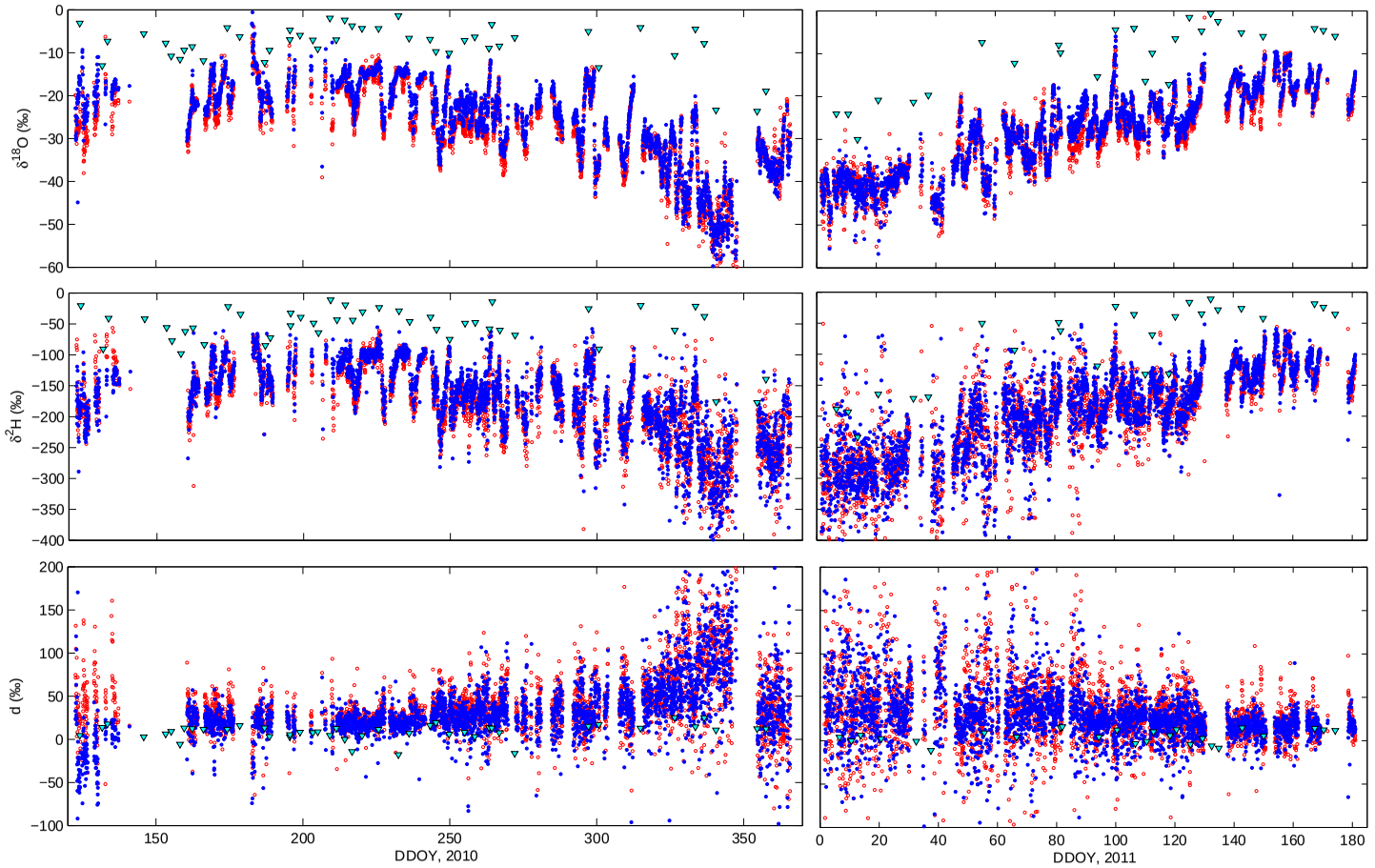

Figure 3.4: Variations in δ^{18}O (top) and δ^{2}H (bottom) in precipitation from January, 2006 through June, 2011.

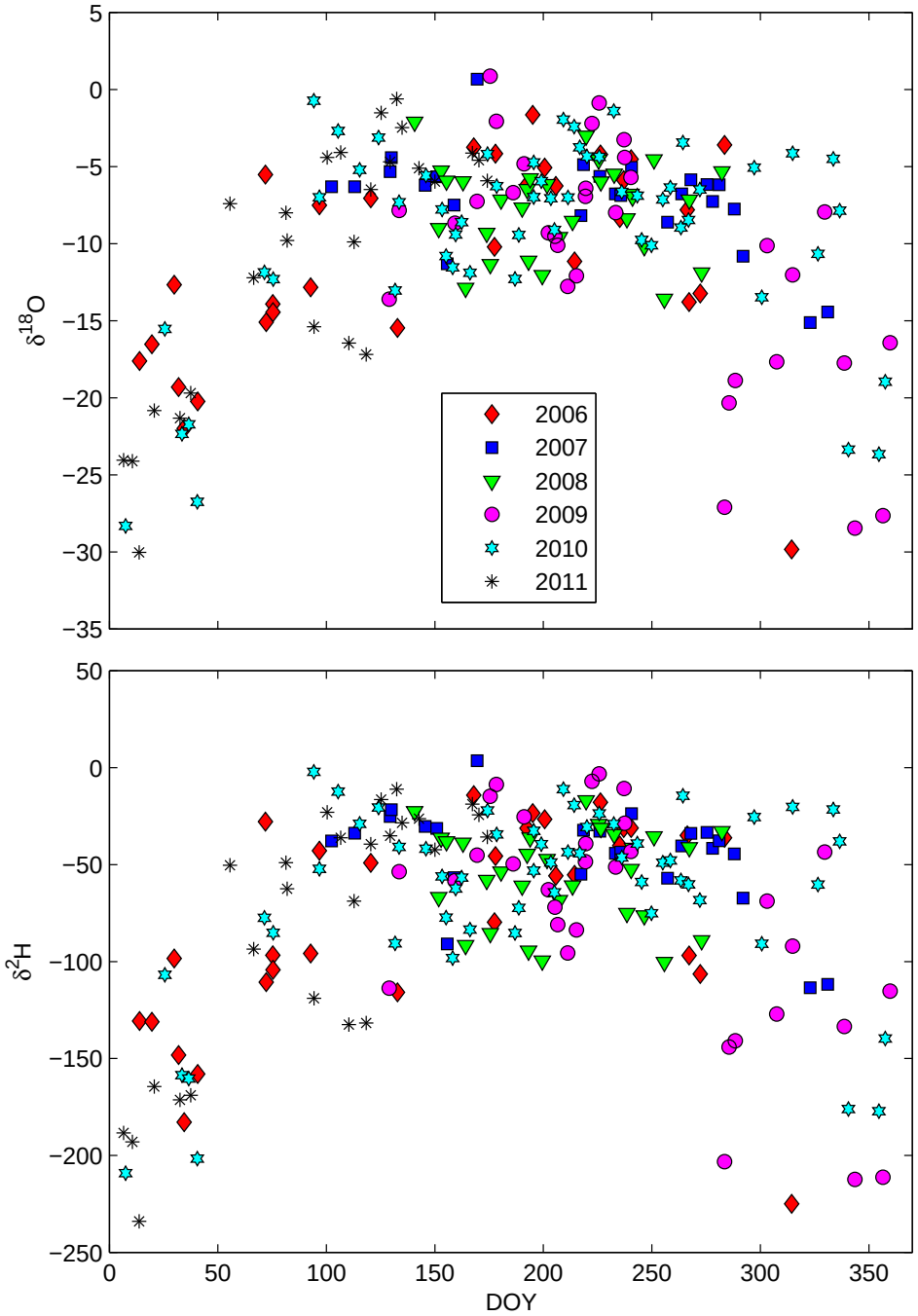

Figure 3.5: Twenty-four hour ensemble average values of δ^{18}O, δ^{2}H, and d at 3m and 185m for four seasons: spring (March-May), summer (June-August), fall (September-November), and winter (December-February). The bottom panel shows the diurnal cycles of the water vapor mixing ratio (w) and relative humidity. The solid lines for 3m and 185m vapor measurements represent a 3 hour moving average.

Figure 3.6: Diurnal variations of ET for four seasons estimated using the average water vapor flux of two field-scale eddy covariance systems in corn and soybean fields within the footprint of the TGO.

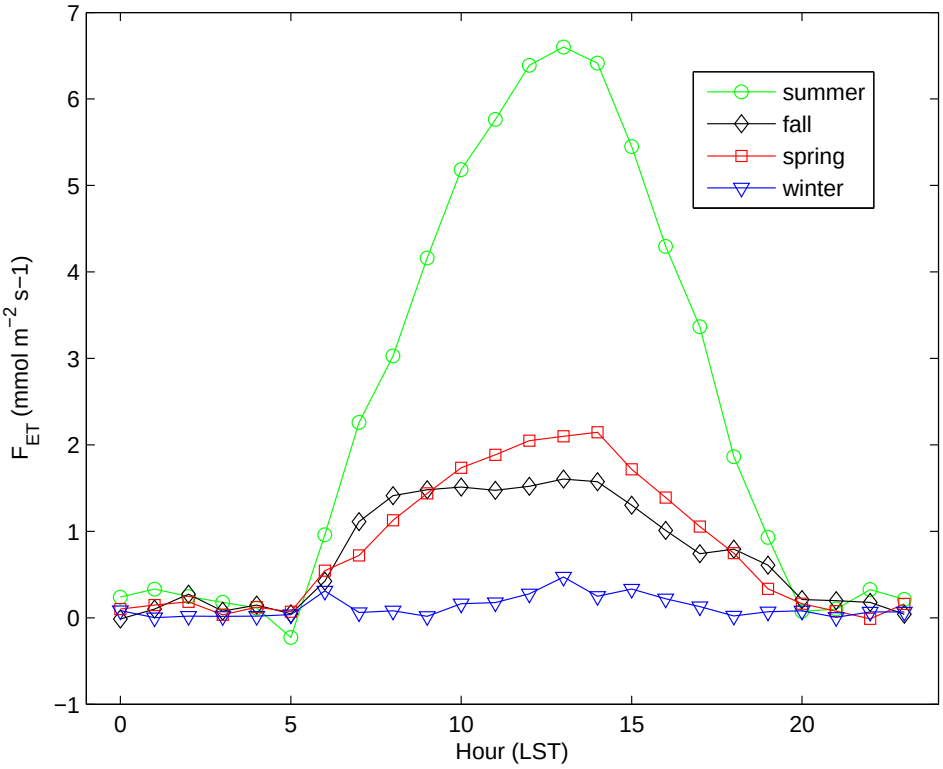

Figure 3.7: The diurnal variations in $\delta^{18}O_{ET}$ (a), $\delta^{2}H_{ET}$ (b), and d_{ET} (c). The dashed lines represent the average value of xylem water collected from corn, soybean, and grass species collected throughout the 2010 growing season within the flux footprint of the tall tower.

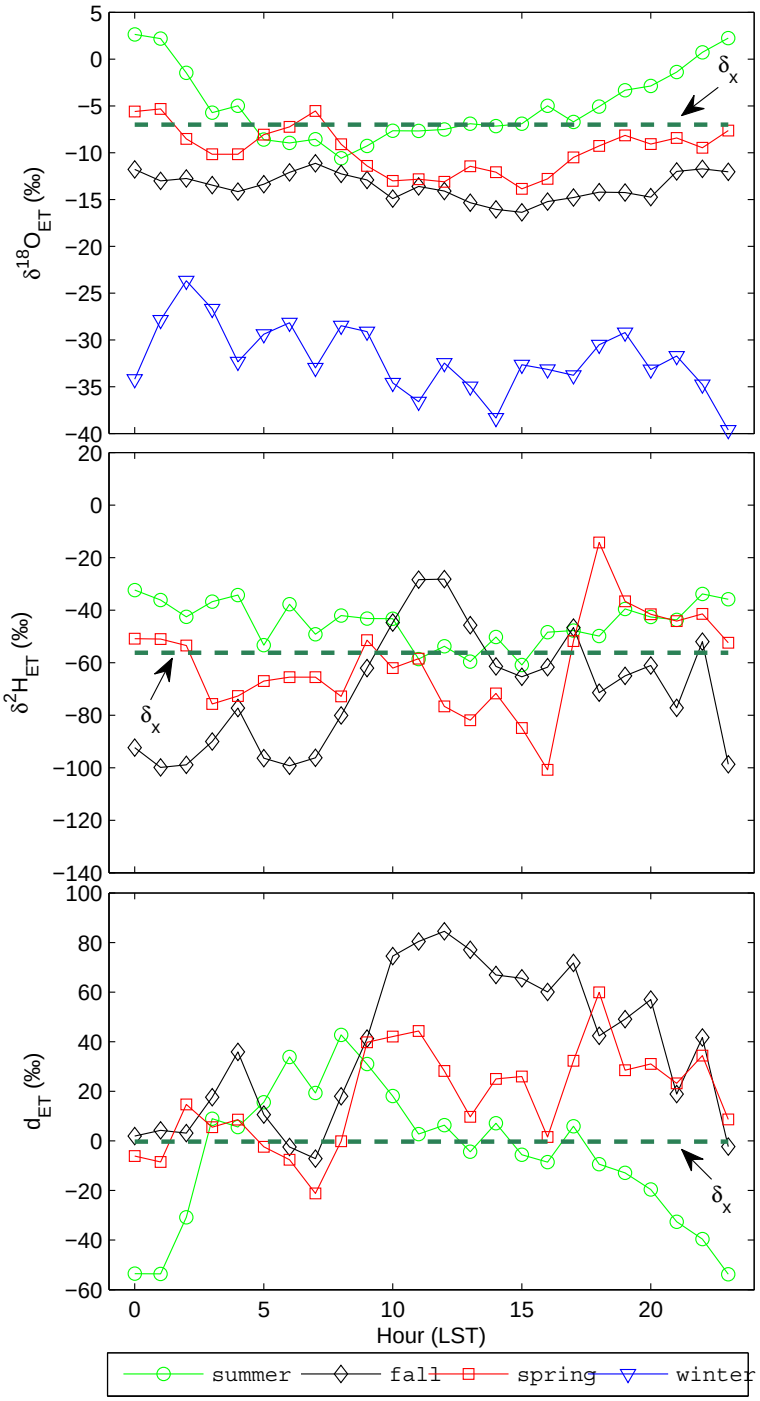

Figure 3.8: The diurnal variations in $I_F\delta^{18}O$ and $I_F\delta^2H$. Evapotranspiration exhibited a positive isoforcing across all seasons, enriching the atmosphere in ^{18}O and ^2H.

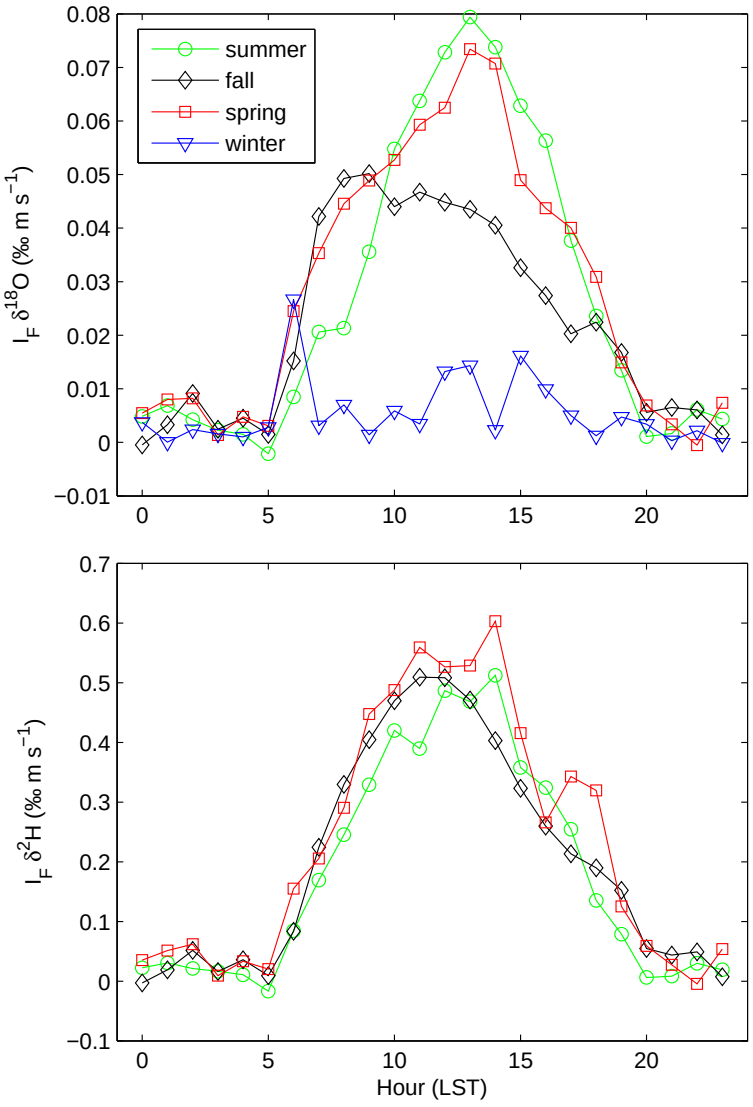

Figure 3.9: Measured values of δ^{18}O, δ^{2}H, and d in water vapor compared with the predicted values of δ^{18}O, δ^{2}H, and d in equilibrium with precipitation.

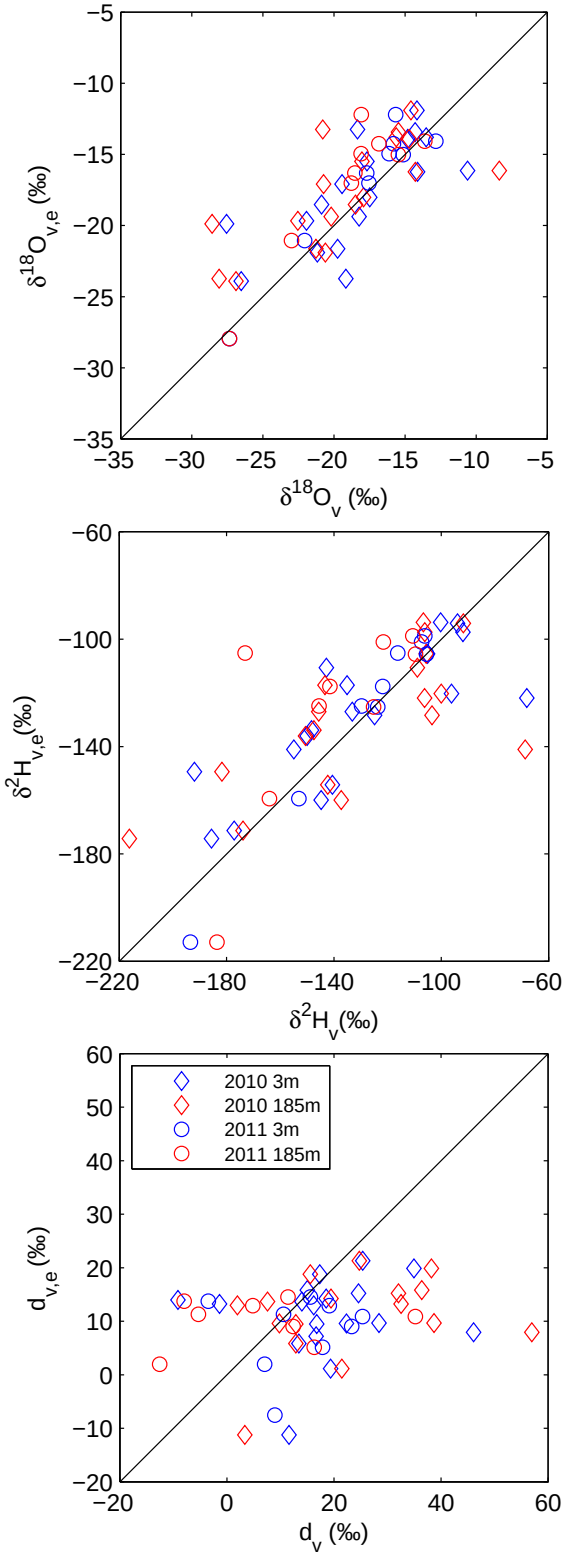

Figure 3.10: The relationship between δ^{18}O and δ^{2}H in water vapor, precipitation, and terrestrial water pools.

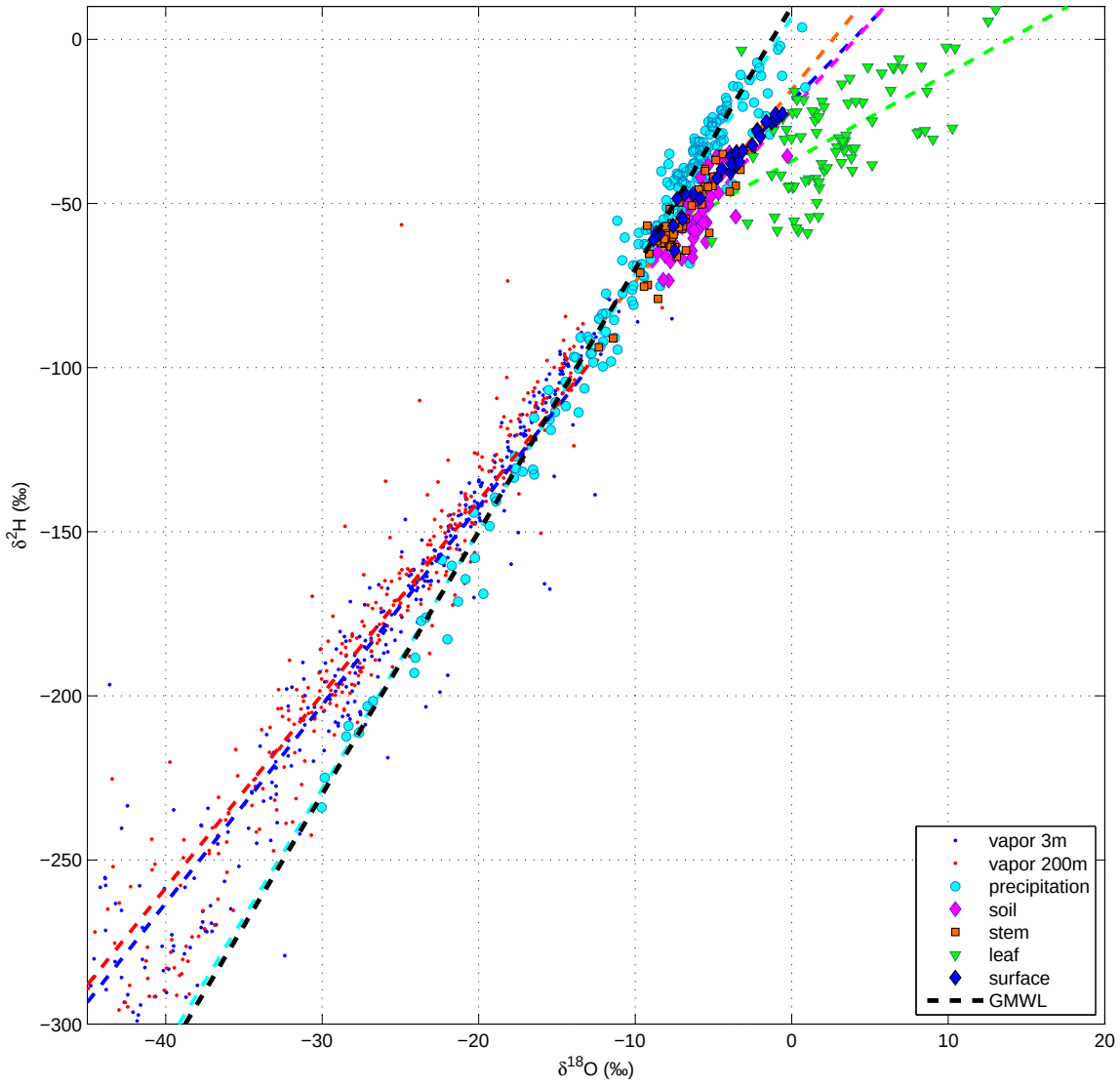

Chapter 4

Thesis Conclusion

The goals of this thesis were to utilize direct measurements of δ^{18}O and δ^{2}H in water vapor on a tall tower in Rosemount, MN, in combination with measurements of the isotope composition of precipitation and terrestrial water pools to develop a landscape-scale understanding of the mechanisms that control variations in the isotope composition of water vapor in the ABL. This type of comprehensive analysis shed insight into the important processes involved in the local and large-scale transport of water, and helps serve as a benchmark in diagnosing future environmental and hydrological changes.

In the first chapter of this thesis, I addressed a technical problem that in the past has prevented the use of isotope ratio infrared spectroscopy (IRIS) analyzers for the isotope analysis of water extracted from plant and soil samples. I performed a correction procedure on an IRIS analyzer to allow for easy isotope analysis of these types of water samples. Because organic molecules (mainly ethanol and methanol) present in plant water absorb in the same wavelengths used to detect the isotopes of hydrogen and oxygen, errors in

the measured ratios of $^{18}O/^{16}O$ and $^{2}H/^{1}H$ occurred. Water extracted from leaves and stems from a variety of 11 plant species were examined. It was found that before the isotope corrections were applied, errors could be as large as 20.8‰ for $\delta^{18}O$, and 34.6‰ for $\delta^{2}H$, making the data unusable. The corrected IRIS isotope values were compared to the same samples analyzed using isotope ratio mass spectrometry (IRMS). There was excellent agreement in $\delta^{18}O$, and much better agreement in $\delta^{2}H$. We believe that this correction method represents a reasonable alternative to IRMS for the isotope analysis of plant and soil waters.

Chapter 1 of this thesis was published in Rapid Communications in Mass Spectrometry in early October. The citation for this paper is: Schultz, N.M., Griffis, T.J., Lee, X., and Baker, J. (2011), Identification and correction of spectral contamination in $^{2}H/^{1}H$ and $^{18}O/^{16}O$ measured in leaf, stem, and soil water, Rapid Communications in Mass Spectrometry, 25, 3360-3368.

In the second chapter of this thesis, I examined how $\delta^{18}O$, $\delta^{2}H$, and *d* measured on the TGO in Rosemount, MN varied over a range of temporal scales, and examined the mechanisms that controlled the variations. Continuous measurements of $\delta^{18}O$ and $\delta^{2}H$ were made at 3m and 185 meters from May 2010 through June 2011. Large seasonal variations were observed in $\delta^{18}O$, $\delta^{2}H$, and *d* resulting from a combination of factors including the rainout effects of distant moisture sources, seasonal temperature variations, and seasonal changes in ET. The diurnal patterns in $\delta^{18}O$ and $\delta^{2}H$ were driven by entrainment of isotopically depleted air from above the ABL, and *d* showed a strong influence

from surface ET. Contrary to a simple Rayleigh model, d was more enriched at 185m than 3m, which requires additional investigation. We hypothesized that the re-evaporation of fog droplets or raindrops could be contributing factors.

Chapter 2 of this thesis has been submitted for publication in the Journal of Geophysical Research - Atmospheres on December 19, 2011.

References

Angert, A., Lee, J., Yakir, D., 2008. Seasonal variations in the isotopic composition of near-surface water vapour in the eastern mediterranean. Tellus 60B, 674–684.

Baker, J., Griffis, T., 2005. Examining strategies to improve the carbon balance of corn/soybean agriculture using eddy covariance and mass balance techniques. Agricultural and Forest Meteorology 128, 163–177.

Bowen, G., Wilkinson, B., 2002. Spatial distribution of δ^{18}O in meteoric precipitation. Geology 30, 315–318.

Brand, W., 2010. Comments on "discrepancies between isotope ratio infrared spectroscopy and isotope ratio mass spectrometry for the stable isotope analysis of plant and soil water". Rapid Communications in Mass Spectrometry 24, 2687–2688.

Brand, W., Geilmann, H., Crosson, E., Rella, C., 2009. Cavity ring-down spectoscopy versus high-temperature conversion isotope ratio mass spectroscometry; a case study of δ^{2}H and δ^{18}O of pure water samples an alcohol/water mixtures. Rapid Communications in Mass Spectrometry 23, 1879–1884.

Cappa, C., Hendricks, M., DePaolo, D., Cohen, R., 2003. Isotopic fractionation of water during evaporation. Journal of Geophysical Research 108, 13.1–13.9.

Craig, H., 1961. Isotopic variations in meteoric waters. Science 133, 1702–1703.

Craig, H., Gordon, L., 1965. Deuterium and oxygen-18 variations in the ocean and the marine atmosphere. In: Tongiorgi, E. (Ed.), Proceedings of a conference on stable isotopes in oceanographic studies and paleotemperatures. pp. 9–130.

Cuntz, M., Ciais, P., Hoffmann, G., Knorr, W., 2003. A comprehensive global three-dimensional model of delta O-18 in atmospheric CO_2: 1. validation of surface processes. Journal of Geophysical Research 108, Art No 4527.

Dai, A., 2006. Recent climatology, variability, and trends in global surface humidity. Journal of Climate 19, 3589–3606.

Dansgaard, W., 1964. Stable isotopes in precipitation. Tellus 16, 436–468.

Draxler, R., Rolph, G., 2010. HYSPLIT (Hybrid Single-Particle Lagrangian Integrated Trajectory) model access via NOAA ARL ready website.
URL `http://ready.arl.noaa.gov/HYSPLIT.php`

Froehlich, K., Kralik, M., Papesch, W., Rank, D., Scheifinger, H., Stichler, W., 2008. Deuterium excess in precipitation of alpine regions - moisture recycling. Isotopes in Environmental and Health Studies 44, 61–70.

Gat, J., 1996. Oxygen and hydrogen isotopes in the hydrological cycle. Annual Review of Earth and Planetary Science 24, 225–262.

Gat, J., 2005. Some classical concepts of isotope hydrology: Rayleigh fractionation, meteoric water lines, the Dansgaard effects, and the d-excess parameter. IEA.

Gat, J., Bowser, C., Kendall, C., 1994. The contribution of evaporation from the great lakes to the continental atmosphere: estimate based on stable isotope data. Geophysical Research Letters 21, 557–560.

Griffis, T., Baker, J., Sargent, S., Erickson, M., Corcoran, J., Chen, M., Billmark, K., 2010a. Influence of C4 vegetation on the $^{13}CO_2$ discrimination and isoforcing in the upper midwest, united states. Global Biogeochemical Cycles 24, GB4006.

Griffis, T., Baker, J., Sargent, S., Tanner, B., Zhang, J., 2004. Measuring field-scale isotopic CO_2 fluxes with tunable diode laser absorption spectroscopy and micrometeorological techniques. Agricultural and Forest Meteorology 124, 15–29.

Griffis, T., Lee, X., Billmark, K., Schultz, N., Erickson, M., Xhang, X., Fassbinder, J., Xiao, W., Hu, N., 2011. Oxygen isotope composition of evapotranspiration and its relation to C4 photosynthetic discrimination. Journal of Geophysical Research 116, G01035.

Griffis, T., Sargent, S., X., L., Baker, J., Greene, J., Erickson, M., Zhang, X., Billmark, K., Schultz, N., Xiao, W., Hu, N., 2010b. Determining the oxygen isotope composition of evapotranspiration using eddy covariance. Boundary Layer Meteorology 137 (2), 307–326.

Groisman, P., Knight, R., Easterling, D., Karl, T., Hergerl, G., Razuvaev, V., 2005. Trends in intense precipitation in the climate record. Journal of Climate 18, 1326–1350.

Gupta, P., Noone, D., Galewsky, J., Sweeney, C., Vaughn, B., 2009. Demonstration of high-precision continuous measurements of water vapor isotopologues in laboratory and remote field deployments using wavelength-scanned cavity ring-down spectroscopy (WS-CRDS) technology. Rapid communications in mass spectrometry 23, 2534–2542.

Hall, A., Manabe, S., 2000. Effect of water vapor feedback on internal and anthropogenic variations of the global hydrologic cycle. Journal of Geophysical Research 105, 6935–6944.

Hansen, J., Ruedy, R., Sato, M., Lo, K., 2010. Global surface temperature change. Review of Geophysics 48, RG4004.

He, H., Smith, R., 1999. Stable isotope composition of water vapor in the atmospheric boundary layer above the forests of new england. Journal of Geophysical Research 104, 11657–11673.

Held, I., Soden, B., 2000. Water vapor feedback and global warming. Annu. Rev. Energy Environ. 25, 441–475.

Horita, J., Rozanski, K., Cohen, S., 2008. Isotope effects in the evaporation of water: a status report of the craig-gordon model. Isotopes in Environmental and Health Studies 44, 23–49.

Hu, L., , Mohr, M., Wells, K., Griffis, T., Helmig, D., Millet, D., 2011. Sources and seasonality of atmospheric methanol based on tall tower measurements in the us upper midwest. Atmospheric Chemistry and Physics 11, 17474.

Huntington, T., 2010. Climate warming-induced intensification of the hydrologic cycle: An assessment of the published record and potential impacts on agriculture. Advances in Agronomy 109, 1–53.

IAEA-WMO, 2006. Global network of isotopes in precipiation. the GNIP database. Accessible at: http://www.iaea.org/water.

Iannone, R., Romanini, D., Cattani, O., Meijer, H., Kerstel, E., 2010. Water isotope ratio (δ^2H and δ^{18}O) measurements in atmospheric moisture using an optical feedback cavity enhanced absorption laser spectrometer. Journal of Geophysical Research 115, D10111.

IPCC, 2007. Climate Change 2007: The Physical Science Basis: Contribution of Working Group I to the Fourth Assessment Report of the Intergovernmental Panel on Climate Change. Cambridge University Press.

Jacob, H., Sonntag, C., 1991. An 8-year record of the seasonal variation of ^{2}H and ^{18}O in atmospheric water vapour and precipitation at heidelberg, germany. Tellus 43B, 291–300.

Jouzel, J., 2007. Water stable isotopes: atmospheric composition and applications in polar ice core studies. Ch. 4.08, pp. 213–243.

Jouzel, J., Stievenard, M., Johnsen, S., Landais, A., Masson-Delmotte, V., Sveinbjornsdottir, A., Vimeux, F., von Grafenstein, U., White, J., 2007. The grip deuterium-excess record. Quaternary Science Reviews 26, 1–17.

Jung, M., Reichstein, M., Ciais, P., Seneviratne, S., Sheffield, J., Goulden, M., Bonan,

G., Cescatti, A., Chen, J., deJeu, R., Dolman, A., Eugster, W., Gerten, D., Gianelle, D., Gobron, N., heinke, J., Kimball, J., Law, B., Montagnani, L., Mu, Q., Mueller, B., Oleson, K., Papale, D., Richardson, A., Roupsard, O., Running, S., Tomelleri, E., Viovy, N., Weber, U., Williams, C., Wood, E., Zaehle, S., Zhang, K., 2010. Recent decline in the global land evapotranspiration trend due to limited moisture supply. Nature 467, 951–954.

Keihl, J., Trenberth, K., 1997. Earth's annual global mean energy budget. Bulletin of the American Meteorological Society 78, 197–208.

Kim, K., 2011. Laboratory and field investigations of stable water isotopes in ecosystems. Ph.D. thesis, Yale University.

Kurita, N., Yamada, H., 2008. The role of local moisture recycling evaluated using stable isotope data from over the middle of the tibetan plateau during the monsoon seasonal. Journal of Hydrometeorology 9, 760–775.

Lai, C., Ehleringer, J., 2011. Deuterium excess reveals diurnal sources of water vapor in forest airborne. Oecologicia 165, 213–223.

Law, B., Falge, E., Gu, L., Baldocchi, D., Bakwin, P., Berbigier, P., Davis, K., Dolman, A., Falk, M., Fuentes, J., Goldstein, A., Granier, A., Grelle, A., 2002. Environmental control over carbon dioxide and water vapor exchange of terrestrial vegetation. Agricultural and Forest Meteorology 113, 97–120.

Lee, X., Fuentes, J., Staebler, R., Neumann, H., 1999. Long-term observation of the

atmospheric exchange of CO2 with a temperate deciduous forest in southern ontario, canada. Journal of Geophysical Research 104, 15975–15984.

Lee, X., Griffis, T., Baker, J., Billmark, K., Kim, K., Welp, L., 2009. Canopy-scale kinetic fractionation of atmospheric carbon dioxide and water vapor isotopes. Global Biogeochemical Cycles 23, GB1002.

Lee, X., Huang, J., Patton, E., 2011. A large-eddy simulation study of water vapour and carbon dioxide isotopes in the atmospheric boundary layer. Boundary Layer Meteorology in press, xx–xx.

Lee, X., Kim, K., Smith, R., 2007. Temporal variations of the $^{18}O/^{16}O$ signal of the whole-canopy transpiration in a temperate forest. Global Biogeochemical Cycles 21, GB3013.

Lee, X., Sargent, S., Smith, R., Tanner, B., 2005. In-situ measurement of water vapour $^{18}O/^{16}O$ isotope ratio for atmospheric and ecological applications. Journal of Atmospheric and Oceanic Technology 22, 555–565.

Lee, X., Smith, R., Williams, J., 2006. Water vapour $^{18}O/^{16}O$ isotopic ratio in surface air in new england, usa. Tellus 58B, 293–304.

Machavaram, M., Krishnamurthy, R., 1995. Earth surface evaporative processes: A case study from the great lakes region of the united states based on deuterium excess in precipitation. Geochemica et Cosmochimica Acta 59, 4279–4283.

Majoube, M., 1971. Fractionnement en oxyene-18 et en deuterium entre l'eau et sa vapeur. Journal de Chimie Physique 10, 1423.

McCarthy, M., Thorne, P., Titchner, H., 2009. An analysis of tropospheric humidity trends from radiosondes. Journal of Climate 22, 5820–5838.

Merlivat, L., Jouzel, J., 1979. Global climatic interpretation of the deuterium-oxygen 18 relationship for precipitation. Journal of Geophysical Research 84, 5029–5033.

Milly, P., Dunne, K., 2001. Trends in evaporation and surface cooling in the Mississippi River basin. Geophysical Research Letters 28, 1219–1222.

NCDC, 2004a. Climate of Minnesota. Tech. rep., National Climatic Data Center.
URL `http://hurricane.ncdc.noaa.gov`

NCDC, 2004b. Climatography of the United States No. 20 1971-2000, station: Rosemount Agri Exp Stn. Tech. rep., National Climatic Data Center.
URL `http://hurricane.ncdc.noaa.gov`

Peng, H., Mayer, B., Harris, S., Krouse, H., 2004. A 10-yr record of stable isotope ratios of hydrogen and oxygen in precipitation at Calgary, Alberta, Canada. Tellus 56B, 147–159.

Petit, J., Jouzel, J., Raynaud, D., Barkov, N., Barnola, J.-M., Basile, I., Bender, M., Chappellaz, J., Davis, M., Delaygue, G., Delmotte, M., Kotlyakov, V., Legrand, M., Lipenkov, V., Lorius, C., Pepin, L., Ritz, C., Saltzman, E., Stievenard, M., 1999. Climate and atmospheric history of the past 420,000 years from the Vostok ice core, Antarctica. Nature 399, 429–436.

Qian, T., Diai, A., Trenberth, K., 2007. Hydroclimatic trends in the mississippi river basin from 1948-2004. Journal of Climate 20, 4599–4614.

Rozanski, K., Araguas-Araguas, L., Gonfiantini, R., 1993. Isotopic patterns in modern global precipitation, Geophysical Monograph 78. In: Climate Change in Continental Isotopic Records. American Geophysical Union, pp. 1–36.

Santer, B., Mears, C., Wentz, F., Taylor, K., Gleckler, P., Wigley, T., Barnett, T., Boyle, J., Bruggemann, W., Gillett, N., Klein, S., Meehl, G., Nozawa, T., Pierce, D., Stott, P., Washington, W., Wehner, M., 2007. Identification of human-induced changes in atmospheric moisture content. PNAS 104, 15248–15253.

Schultz, N., Griffis, T., Lee, X., Baker, J., 2011. Identification and correction of spectral contamination in $^{2}H/^{1}H$ and $^{18}O/^{16}O$ measured in leaf, stem, and soil water. Rapid Communications in Mass Spectrometry 25, 3360–3368.

Seeley, M., 2010. Climate change in minnesota: Current trends and projections. In: Clean Water and Climate Adaptation Summit.

Shurpali, N., Verma, S., 1998. Micrometeorological measurements of methane flux in a minnesota peatland during two growing seasons. Biogeochemistry 40, 1–15.

Steffensen, J., Andersen, K., Bigler, M., Clausen, H., Dahl-Jensen, D., Fischer, H., Goto-Azuma, K., Hansson, M., Johnsen, S., Jouzel, J., Masson-Delmotte, V., Popp, T., Rasmussen, S., Rothlisberger, R., Ruth, U., Stauffer, B., Siggard-Andersen, M., Sveinbjornsdottir, A., Svensson, A., White, J., 2008. High-resolution Greenland ice core data show abrupt climate change happens in a few years. Science 321, 680–683.

Stewart, M., 1975. Stable isotope fractionation due to evaporation and isotopic exchange of falling water drops: applications to atmosphereic processes and evaporation of lakes. Journal of Geophysical Research 80, 1133–1146.

Sturm, P., Knohl, A., 2010. Water vapor δ^2H and δ^{18}O measurements using off-axis integrated cavity output spectroscopy. Atmospheric Measurement Techniques 3, 67–77.

Trenberth, K., 2011. Changes in precipitation with climate change. Climate Research 47, 123–138.

Trenberth, K., Fasullo, J., Smith, L., 2005. Trends and variability in column-integrated atmospheric water vapor. Climate Dynamics 24, 741–758.

Uemura, R., Matsui, Y., Yoshimura, K., Motoyama, H., Yoshida, N., 2008. Evidence of deuterium excess in water vapor as an indicator of ocean surface conditions. Journal of Geophysical Research 113, D19114.

Vachon, R., Welker, J., White, J., Vaughn, B., 2010. Moisture source temperatures and precipitation δ^{18}O - temperature relationships across the United States. Water Resources Research 46, W07523.

Walter, M., Wilks, D., Parlange, J.-Y., Schneider, R., 2004. Increasing evapotranspiration from the conterminous united states. Journal of Hydrometeorology 5, 405–408.

Wang, L., Caylor, K., Villegas, J., Barron-Gafford, G., Breshears, D., Huxman, T., 2010.

Partitioning evapotranspiration with woody plant cover: Assessment of a stable isotope technique. Geophysical Research Letters 37, L09401.

Welker, J., 2000. Isotopic (delta 18o) characteristics of weekly precipitation collected across the usa: an initial analysis with application to water source studies. Hydrological Processes 14, 1449–1464.

Welp, L., Lee, X., Griffis, T., Wen, X., Xiao, W., Li, S., Sun, X., Hu, Z., 2011. A meta-analysis of deuterium-excess in water vapor in the atmospheric surface layer in mid-latitudes. Global Biogeochemical Cycles in review, xxx–xxx.

Welp, L., Lee, X., Kim, K., Griffis, T., Billmark, K., Baker, J., 2008. δ^{18}O of water vapour, evapotranspiration and the sites of leaf water evaporation in a soybean canopy. Plant, Cell and Environment 31, 1214–1228.

Wen, X., Sun, X., Zhang, S., Yu, G., Sargent, S., Lee, X., 2008. Continuous measurement of water vapor D/H and ^{18}O/^{16}O isotope ratios in the atmosphere. Journal of Hydrology 349, 489–500.

Wen, X., Zhang, S., Sun, X., Yu, G., Lee, X., 2010. Water vapor and precipitation ratios in Beijing, China. Journal of Geophysical Research-Atmospheres 115, D01103.

West, A., Goldsmith, G., Brooks, P., Dawson, T., 2010. Discrepancies between isotope ratio infrared spectroscopy and isotope ratio mass spectrometry fro the stable isotope analysis of plant and soil waters. Rapid Communications in Mass Spectrometry 24, 1948–1954.

West, A., Goldsmith, G., Matimati, I., Dawson, T., 2011. Spectral analysis software improves confidence in plant and soil water stable isotope analyses performed by isotope ratio infrared spectroscopy (iris). Rapid Communications in Mass Spectrometry 25, 2268–2274.

West, A., Hultine, K., Burtch, K., Ehleringer, J., 2007. Season variations in moisture use in a pinon-juniper woodland. Oecologica 153, 787–798.

West, A., Patrickson, S., Ehleringer, J., 2006. Water extraction times for plant and soil materials used in stable isotope analysis. Rapid Communications in Mass Spectrometry 20, 1317–1321.

Williams, D., Cable, W., Hultine, K., Hoedjes, J., Yepez, E., Simonneaux, V., Er-Raki, S., Boulet, G., de Bruin, H., Chehbouni, A., Hartogensis, O., Timouk, F., 2004. Evapotranspiration components determined by stable isotope, sap flow, and eddy covariance techniques. Agricultural and Forest Meteorology 125, 241–258.

Worden, J., Noone, D., Bowman, K., 2007. Importance of rain evaporation and continental convection in the tropical water cycle. Nature 445, 528–532.

Wright, W., Leavitt, S., 2006. Boundary layer humidity reconstruction for a semiarid localtion from tree ring cellulose δ^{18}O. Journal of Geophysical Research 111, D18105.

Yakir, D., Wang, X.-F., 1996. Fluxes of co2 and water between terrestrial vegetation and the atmosphere estimated from isotope measurements. Nature 380, 515–517.

Yamanaka, T., Shimizu, R., 2007. Spatial distribution of deuterium in atmospheric water

vapor: Diagnosing sources and the mixing of atmospheric moisture. Geochemica et Cosmochimica Acta 71, 3162–3169.

Zhang, W., Cheng, B., Hu, Z., An, S., Xu, Z., Zhao, Y., Cui, J., Xu, Q., 2010. Using stable isotopes to determine the water sources in alpine ecosystems on the east qinghai-tibet plateau, china. Hydrological Processes 24, 3270–3280.

Zhao, L., Xiao, H., Zhous, J., Wang, L., Cheng, G., Zhou, M., Yin, L., McCabe, M., 2011. Detailed assessment of isotope ratio infrared spectroscopy and isotope ratio mass spectrometry for the stable isotope analysis of plant and soil waters. Rapid Communications in Mass Spectrometry 25, 3071–3082.